Transient Responses of a Coupled Ocean–Atmosphere Model to Gradual Changes of Atmospheric CO_2. Part I: Annual Mean Response

S. MANABE, R. J. STOUFFER, M. J. SPELMAN AND K. BRYAN

Geophysical Fluid Dynamics Laboratory/NOAA, Princeton University, Princeton, New Jersey

(Manuscript received 2 November 1990, in final form 4 March 1991)

ABSTRACT

This study investigates the response of a climate model to a gradual increase or decrease of atmospheric carbon dioxide. The model is a general circulation model of the coupled atmosphere–ocean–land surface system with global geography and seasonal variation of insolation. To offset the bias of the coupled model toward settling into an unrealistic state, the fluxes of heat and water at the ocean–atmosphere interface are adjusted by amounts that vary with season and geography but do not change from one year to the next. Starting from a quasi-equilibrium climate, three numerical time integrations of the coupled model are performed with gradually increasing, constant, and gradually decreasing concentration of atmospheric carbon dioxide.

It is noted that the simulated response of sea surface temperature is very slow over the northern North Atlantic and the Circumpolar Ocean of the Southern Hemisphere where vertical mixing of water penetrates very deeply. However, in most of the Northern Hemisphere and low latitudes of the Southern Hemisphere, the distribution of the change in surface air temperature of the model at the time of doubling (or halving) of atmospheric carbon dioxide resembles the equilibrium response of an atmospheric–mixed layer ocean model to CO_2 doubling (or halving). For example, the rise of annual mean surface air temperature in response to the gradual increase of atmospheric carbon dioxide increases with latitudes in the Northern Hemisphere and is larger over continents than oceans.

When the time-dependent response of the model oceans to the increase of atmospheric carbon dioxide is compared with the corresponding response to the CO_2 reduction at an identical rate, the penetration of the cold anomaly in the latter case is significantly deeper than that of the warm anomaly in the former case. The lack of symmetry in the penetration depth of a thermal anomaly between the two cases is associated with the difference in static stability, which is due mainly to the change in the vertical distribution of salinity in high latitudes and temperature changes in middle and low latitudes.

Despite the difference in penetration depth and accordingly, the effective thermal inertia of the oceans between the two experiments, the time-dependent response of the global mean surface air temperature in the CO_2 reduction experiment is similar in magnitude to the corresponding response in the CO_2 growth experiment. In the former experiment with a colder climate, snow and sea ice with high surface albedo cover a much larger area, thereby enhancing their positive feedback effect upon surface air temperature. On the other hand, surface cooling is reduced due to the larger effective thermal inertia of the oceans. Because of the compensation between these two effects, the magnitude of surface air temperature response turned out to be similar between the two experiments.

1. Introduction

It is well known that oceans spread the heat trapped by greenhouse gases downward, thereby reducing the rate of warming of the oceanic surface. The role of the oceans in determining the rate of warming induced by greenhouse gases has been the subject of several studies (Hoffert et al. 1980; Bryan et al. 1982, 1988; Thompson and Schneider 1982; Hansen et al. 1984, 1988; Spelman and Manabe 1984; Harvey and Schneider 1985; Schlesinger et al. 1985; Washington and Meehl 1989; Stouffer et al. 1989; and Manabe et al. 1990). These studies indicate that oceans can have a major influence upon the rate and the distribution of climate change. However, a major effort is required to elucidate the specific dynamical mechanisms that control the greenhouse warming of climate. The present study is the extension of the study of Stouffer et al. (1989) in which the transient response of climate to a gradual increase of atmospheric carbon dioxide was investigated by use of a coupled ocean–atmosphere model with global computational domain and seasonal variation of insolation.

In the present study, the results of Stouffer et al. (1989) are described in detail and are compared with another experiment in which atmospheric carbon dioxide is reduced with time at an identical rate. In the case of a simple linear model (Hoffert et al. 1980), it is expected that the two antisymmetric CO_2 forcing experiments would yield responses opposite in sign but

Corresponding author address: Dr. Syukuro Manabe, Geophysical Fluid Dynamics Lab, Princeton University, Forrestal Campus, U.S. Route 1, P.O. Box 308, Princeton, NJ 08542.

qualitatively similar in distribution. The confirmation of this expectation should enhance our confidence in the results of the numerical experiments. However, one also has to recognize that these two antisymmetric forcings may not yield exactly antisymmetric responses. As shown in this study, the vertical distributions of both temperature and salinity are altered, thereby changing the static stability of the upper oceanic layer of the model in opposite directions. Thus, the penetration depths of the positive and negative anomalies in the model oceans are not the same. By evaluating the difference in penetration depth and its effect upon the temporal variation of climate between the two experiments, it is hoped to elucidate the nonlinearity of the processes that control the CO_2-induced, time-dependent variation of climate.

So far, most of the modeling studies of greenhouse warming have been conducted by computing the so-called equilibrium response of a climate model to a doubling or quadrupling of atmospheric carbon dioxide. The equilibrium response is the change of climate achieved over an infinite length of time and represents the full response of climate to a given change of atmospheric carbon dioxide without the delay or reduction due to the thermal inertia of the oceans. Thus, its distribution may be substantially different from that of the transient response, which is influenced by the large thermal inertia of the oceans. Such a possibility was emphasized by Thompson and Schneider (1982) by noting the large interhemispheric asymmetry in oceanic area coverage. The present study conducts an extensive comparison between the time-dependent response of the coupled ocean–atmosphere model obtained by Stouffer et al. (1989) with the equilibrium response of another model in which the atmospheric model is combined with a simple mixed layer model of the oceans. In this latter model, the heat exchange between the mixed layer and deeper oceanic layer is prescribed such that the seasonal and geographic distribution of sea surface temperature is realistic in the control run. An identical heat flux is also prescribed in the doubled and halved CO_2 runs. This is in contrast to the transient response of the coupled ocean–atmosphere model in which the heat exchange between the mixed layer and deeper ocean layers changes with time. By comparing the equilibrium and transient responses, the present study explores how ocean currents spread downward the heat trapped by the gradually increasing atmospheric carbon dioxide, thereby reducing the warming of the sea surface and altering the climate response.

2. Coupled ocean–atmosphere model

The coupled ocean–atmosphere model used for this study consists of a general circulation model of the world ocean coupled to a general circulation model of the atmosphere. Heat and water budgets of the continental surface are included. The model has global geography consistent with its computational resolution and seasonally varying insolation. It is very similar to the model used by Manabe et al. (1990) except that the seasonal variation of insolation is taken into account.

In the atmospheric component of the model, the dynamic computation is performed using a spectral transform method in which the horizontal distribution of a predicted variable is represented by a truncated series of spherical harmonics and grid point values (Gordon and Stern 1982). The resolution is limited by a cutoff beyond zonal wavenumber 15. The same number of degrees of freedom is used in representing the latitudinal distribution of each zonal wave component. The effects of clouds, water vapor, carbon dioxide, and ozone are included in the calculation of solar and terrestrial radiation. The distribution of water vapor is predicted in the model, but the mixing ratio of carbon dioxide is assumed to be constant throughout the model atmosphere. Ozone is specified as a function of latitude and height from observations. Overcast cloud is assumed whenever the relative humidity of air exceeds a critical value (99%). Otherwise, clear sky is predicted. As noted above, the insolation imposed at the top of the atmosphere has seasonal variation. However, its diurnal variation is removed for the sake of simplicity and economy of computation. The solar constant is assumed to be 1353 W m^{-2}.

Precipitation is simulated whenever supersaturation is indicated by the prognostic equation for water vapor. The precipitation is identified as snowfall when the air temperature near the surface falls below freezing; otherwise it is identified as rain. Moist convective processes are parameterized by a moist convective adjustment scheme as described in Manabe et al. (1965).

The computation of land surface temperature satisfies the constraint of no surface heat storage. That is, the contributions from net fluxes of solar and terrestrial radiation and turbulent fluxes of sensible and latent heat must balance locally and continuously. The albedo distribution of snow-free surfaces is determined by referring to the study of Posey and Clapp (1964). When the surface is covered by snow, the albedo is replaced by a higher value depending on surface temperature and snow depth. For deep snow (water equivalent at least 2 cm), the surface albedo is 60% if the surface temperature is below −10°C and 45% at 0°C with a linear interpolation between these values from −10° to 0°C. When the water equivalent of the snow depth is less than 2 cm, it is assumed that the albedo decreases from the deep snow values to the albedo of the underlying surface as a square root function of snow depth.

The change in snow depth is computed as the contribution of snowfall, sublimation, and snowmelt, which is determined from the requirement of surface heat balance [see Manabe (1969) for further details].

The budget of soil moisture is computed by the so-

called bucket method (Manabe 1969). Within the model, soil is assumed to have the ability to contain 15 cm of liquid water. When soil is not saturated with water, the change of soil moisture is predicted as the net contribution of rainfall, evaporation, and snowmelt. If the soil moisture value reaches the field capacity of 15 cm, the excess water is regarded as runoff. The rate of evaporation from the soil surface is determined as a function of the water content of the "bucket" and potential evaporation, i.e., the hypothetical evaporation rate from a completely wet surface.

The basic structure of the oceanic component of the model is similar to the model described by Bryan and Lewis (1979). The primitive equations of motion are constructed by use of Boussinesq, rigid-lid, and hydrostatic approximations. Subgrid scale motion is included as turbulent viscosity or turbulent diffusion. Whenever the vertical stratification in the model oceans is unstable, it is assumed that the coefficient of vertical diffusion becomes infinitely large, and the vertical gradients of both temperature and salinity are removed. This process of convective adjustment, together with the large-scale sinking of dense water, contributes to the formation of deep water in the model oceans. For further details on the parameterization of the effect of subgrid scale mixing, refer to appendix A.

The finite difference mesh of the oceanic component of the model has a spacing between grid points of 4.5° latitude and 3.75° longitude. It has 12 levels for the finite differencing in the vertical direction. The computational resolution specified above is marginally adequate for representing coastal currents but cannot describe mesoscale eddies.

Because of the coarse horizontal resolution of the model, many features of bottom topography are only crudely resolved. For example, the mid-Atlantic Ridge of the model is not as high above the sea floor as observed; also Iceland is eliminated. To computationally resolve the ocean currents passing through the narrow Drake Passage, the meridional span of the passage in the upper oceanic layers is expanded to four grid intervals, i.e., 2000 km. No attempt is made to resolve the flow through the Strait of Gibraltar. Instead, the water at the westernmost Mediterranean grid point is mixed horizontally and completely with the water at the adjacent Atlantic grid point to a depth of 1350 meters. [See Fig. 2 of Manabe et al. (1990) for the map of bottom topography.] No net flow is permitted through the Bering Strait.

The prognostic system of sea ice is similar to the very simple free drift model developed by Bryan (1969). The sea ice moves freely with the surface ocean currents provided that its thickness is less than 4 m, but is stationary for higher values. Following Broccoli and Manabe (1987), the albedo of sea ice depends on surface temperature and ice thickness. For thick sea ice (at least 1 m thick), the surface albedo is 80% if the surface temperature is below −10°C and 55% at 0°C, with a linear interpolation between these values for intermediate temperatures. If the ice thickness is less than 1 m, the albedo decreases with a square root function of ice thickness from the thick ice values to the albedo of the underlying water surface.

The atmospheric and oceanic components interact with each other through exchanges of heat, water, and momentum. The heat exchange is accomplished by the net radiative flux and turbulent fluxes of sensible and latent heat. The water (or ice) exchange consists of evaporation (or sublimation), rainfall (or snowfall), and runoff from the continents. The runoff flows in the direction of steepest descent based on the specified topography. Glacier flow is computed in a similar manner. To prevent indefinite growth of an ice sheet through snow accumulation, it is assumed that the water equivalent depth of snow does not exceed 20 cm and the excess snow also runs off by glacial flow in the direction of the steepest descent and instantly reaches the oceans. The ocean surface temperature and sea ice predicted in the ocean are used as lower boundary conditions for the atmosphere. Details of the heat, moisture, and momentum exchange processes are given, for example, by Manabe (1969).

3. Transient response experiments

a. Numerical experiments

To study the response of a coupled ocean–atmosphere model to a gradual increase (or reduction) of atmospheric carbon dioxide, three 100-year integrations of the model were performed as illustrated schematically in Fig. 1. Starting from an initial condition, which is in a quasi-equilibrium state described in section 3b, the standard time integration of the coupled ocean–atmosphere model (hereafter referred to as the S integration) was performed with a normal concentration of atmospheric carbon dioxide. In addition, two 100-year integrations were performed from the identical initial condition. In one integration, the CO_2 concentration in the atmosphere increased by 1%/year (compounded), whereas it is reduced by the identical rate in the other integration. The rate of 1%/year is chosen because the total CO_2-equivalent radiative forcing of various greenhouse gases other than water vapor is currently increasing at the rate of approximately 1%/year [see, for example, Hansen et al. (1988) on the current trace gas trends]. For convenience, these two integrations with growing and decreasing CO_2 concentration are identified as G and D integrations, respectively. The influences of a gradual increase and a gradual reduction of atmospheric carbon dioxide are evaluated by computing the differences between the G and S integrations and the D and S integrations, respectively. Accordingly, these two pairs of integrations will be identified as the CO_2 growth and CO_2 reduction experiments.

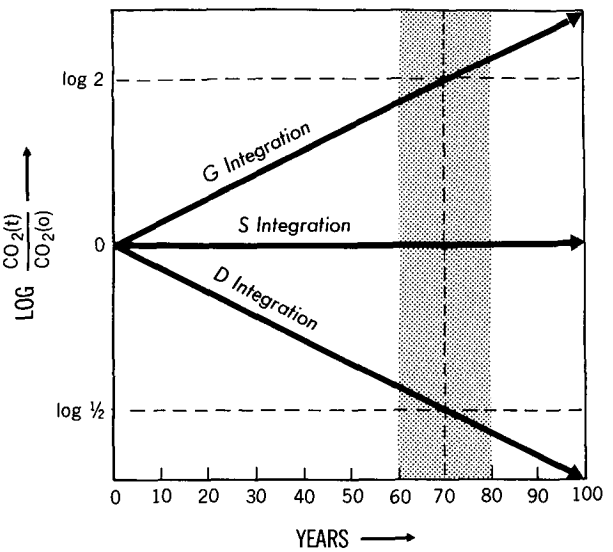

FIG. 1. Schematic diagram of the G, S, and D integrations. The abscissa denotes time in years and the ordinate is the logarithm of the ratio of atmospheric carbon dioxide at time t to its initial value. The period chosen for detailed analysis is indicated by shading.

Since the infrared absorptivity (or emissivity) of carbon dioxide is approximately proportional to the logarithm of its amount, the exponentially growing and decreasing concentration of carbon dioxide exerts thermal forcings that are similar in magnitude but have opposite sign. Thus, it is of interest to see whether the responses of the coupled model to such antisymmetric forcings are opposite in sign, but are similar in magnitude, indicating a linear relationship between the thermal forcing and the response of the model. On the other hand, if the responses of the coupled model to these two forcings significantly deviate from antisymmetry, it suggests that the coupled model responds nonlinearly to these forcings.

b. Initial condition and time integrations

When the time integration of a model starts from an initial condition that is not in equilibrium, the model climate usually undergoes a rapid drift toward the equilibrium state. Such a drift contaminates the CO_2-induced, time-dependent response of climate, which is the subject of the present study. Thus, it is highly desirable that the initial condition for the time integrations conducted here be as close to the state of equilibrium as possible.

Recently Manabe and Stouffer (1988) have shown that a time integration of the original version of their model without using flux adjustments yielded an unrealistic equilibrium state, characterized by an intense halocline in high latitudes and the absence of a significant thermohaline circulation in the North Atlantic. In order to offset this bias, they adjusted the flux of water at the oceanic surface by an amount that varies geographically but does not change during the integration of the model. Performing this adjustment, they obtained two stable equilibria with and without a significant thermohaline circulation in the Atlantic Ocean, depending upon the initial conditions chosen. Although the latter equilibrium resembles the state obtained earlier without the adjustment, the former equilibrium with the thermohaline circulation is similar to the current condition in the Atlantic Ocean. In the present study, such an adjustment is performed for both water and heat fluxes. The adjustments have no interannual variation and are independent of the temporal variation of the model climate. The initial condition for the time integration and the distributions of the flux adjustments are determined from separate integrations of the atmospheric and oceanic components of the model. These preliminary integrations, as well as the synchronous integration of the coupled model, are described below.

1) ATMOSPHERIC LEG OF THE PRELIMINARY INTEGRATION

Starting from the initial condition of an isothermal and dry atmosphere at rest, the atmospheric component of the model is time integrated over the period of 12 years with the seasonally and geographically varying, observed sea surface temperature and sea ice as a lower boundary condition. For this purpose, the seasonally varying, geographical distribution of sea ice thickness is estimated from satellite observations of sea ice concentration (Parkinson et al. 1987; Zwally et al. 1983).

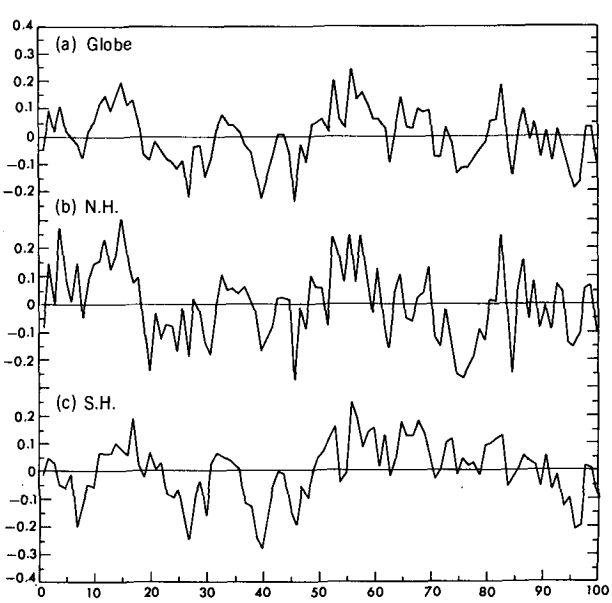

FIG. 2. The temporal variations of area-averaged deviation of annual mean surface air temperature (°C) from the 100-year mean temperature produced by the S integration of the coupled model for (a) globe, (b) Northern Hemisphere, (c) Southern Hemisphere.

During the last 10 years of this integration, the model atmosphere attained a quasi-steady state in which its seasonal variation nearly repeats itself. The atmospheric state reached at the end of the integration is then used as the atmospheric part of the initial condition for the integration of the coupled ocean–atmosphere model. For the determination of the flux adjustments mentioned above, the seasonal and geographical distributions of the net downward fluxes of heat and moisture at the oceanic surface are obtained by averaging over the last 10 annual cycles of the atmospheric leg. The corresponding distribution of surface momentum flux is also computed to be used as an upper boundary condition for the oceanic leg of the preliminary integration described below.

2) Oceanic leg of the preliminary integration

The oceanic component of the model is time integrated over the period of 2400 years. The surface temperature and salinity are relaxed toward the observed values, which vary seasonally and geographically. The relaxation time is chosen to be 50 days, which is short enough to prevent significant deviation of the surface condition from the observed. The distribution of surface flux of momentum from the atmospheric leg of the integration is also imposed. In this time integration, the approach of the deeper layers of the model ocean toward the state of equilibrium is accelerated as described by Bryan et al. (1975) and Bryan (1984), thereby extending the effective length of time integration to 34 000 years. Toward the end of this integration there is little systematic trend in the temporal variation of the oceanic state. The oceanic state, which is reached at the end of this integration, is used as the oceanic part of the initial condition for the time integrations of the coupled ocean–atmosphere model. In addition, seasonal and geographical distributions of the surface fluxes of water and heat, needed to maintain the realistic distributions of imposed sea-surface temperature, surface salinity, and sea ice are also computed from the last 500 annual cycles. These fluxes are used for

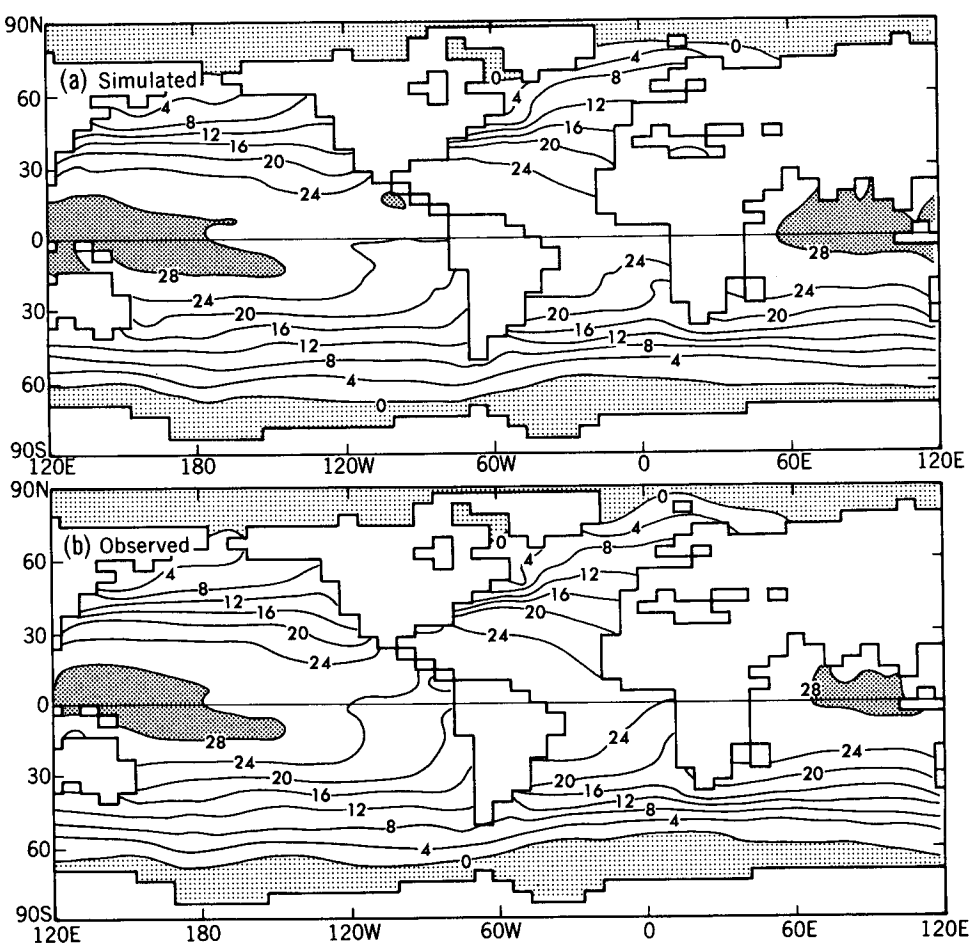

FIG. 3. Geographical distribution of annual-mean sea surface temperature (°C). (a) The simulated distribution of the temperature averaged over the 100-year period of the S integration of the coupled model. (b) The observed distribution from Levitus (1982).

the determination of flux adjustments in the time integration of the coupled ocean–atmosphere model as described below.

3) Synchronous integrations of the coupled ocean–atmosphere model

The initial condition for the S, G, and D integrations of the coupled ocean–atmosphere model identified earlier is constructed by combining the states reached at the end of the atmospheric and oceanic legs of the time integrations described above. Because of the imperfections of the model (Appendix B), the distributions of the surface fluxes of heat and water, obtained from the atmospheric leg of the preliminary integration with realistic sea surface temperature and sea ice, differ from the annual cycles of these fluxes, which are needed to maintain the realistic surface condition in the oceanic leg of the integration. To prevent a systematic drift of climate due to this inconsistency, the surface fluxes of water and heat (but not of momentum) from the atmospheric component of the model are modified by amounts equal to the difference between the two sets of fluxes derived in the preliminary integrations before they are imposed upon the oceanic component. (See appendix B for the magnitude and the latitudinal distributions of the adjustments.) Although the adjustment of a flux depends upon season and geographical location, it does not change from one year to the next. Nevertheless, the state of the coupled model remains near the initial quasi-equilibrium condition in the standard S integration as shown in the next section, underscoring its stability. Identical adjustments of heat and water fluxes are also imposed in both the G and D integrations.

4. Equilibrium response experiments

As noted in the Introduction, one of the main goals of the present study is to investigate how the oceans affect the response of climate to a change of atmospheric carbon dioxide. For this purpose, one can

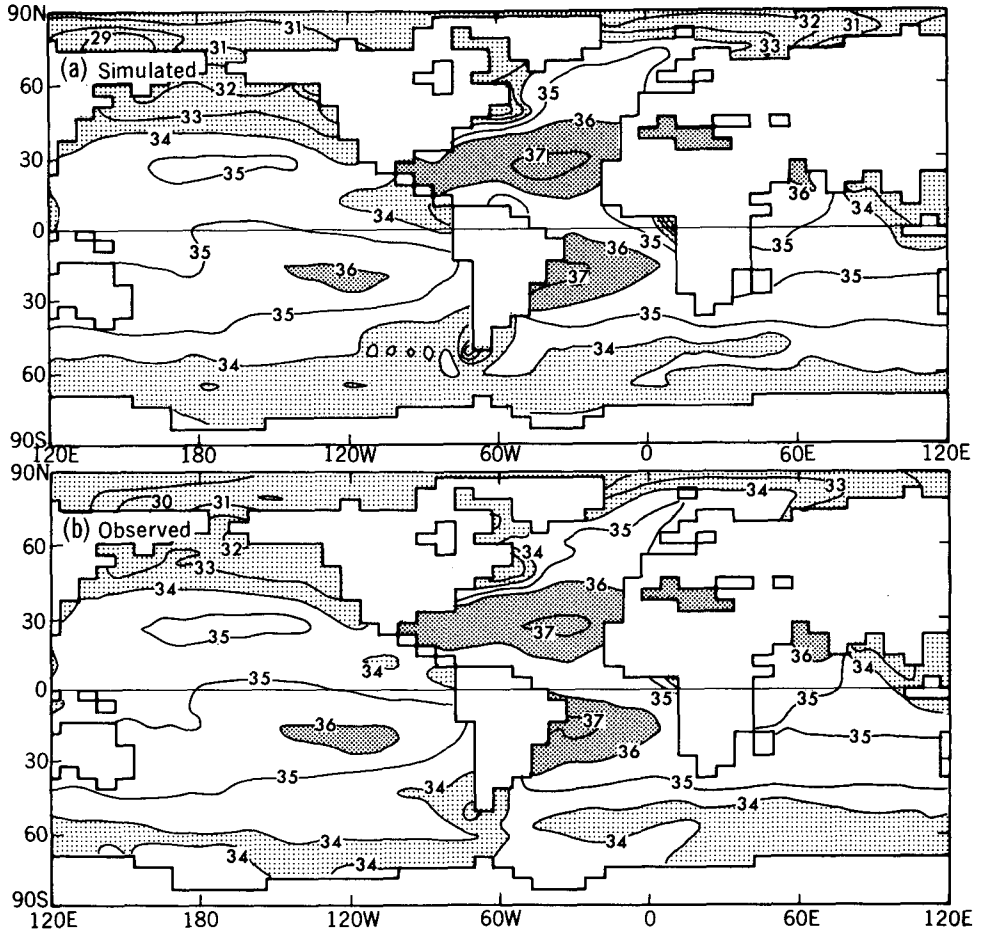

FIG. 4. Geographical distribution of annual-mean sea surface salinity (psu). (a) The simulated distribution of the salinity averaged over the 100-year period of the S integration. (b) The observed distribution from Levitus (1982).

compare the transient response of the coupled ocean–atmosphere model to the equilibrium response of the same model. Such a comparison has been made in several studies conducted at the Geophysical Fluid Dynamics Laboratory of NOAA (Bryan et al. 1982, 1988; Spelman and Manabe 1984; Manabe et al. 1990). These studies, however, investigated the transient response to an abrupt doubling rather than the response to a gradual change of atmospheric carbon dioxide, which is the main subject of the present study.

a. The atmosphere–mixed-layer ocean model

As explained in the Introduction, the model used for the equilibrium response experiment in the present study differs from the coupled ocean–atmosphere model used for the transient response experiment. Although its atmospheric and land-surface components are identical to those of the coupled ocean–atmosphere model, its oceanic component is a simple mixed-layer ocean model, which is a 50-m thick slab of vertically well-mixed water. The oceanic component contains a highly idealized scheme for sea-ice prediction, which is identical to the thermodynamical part of the sea-ice scheme used in the coupled ocean–atmosphere model. The rate of heat exchange between the mixed layer and the deep ocean layers is prescribed such that the seasonal and geographical distributions of sea surface temperature and sea-ice thickness are realistic. This model will hereafter be identified as the atmosphere–mixed-layer ocean model or, more simply, as the AM model.

b. Preliminary integration

In order to determine the heat flux to be prescribed at the bottom of the mixed-layer ocean of the AM

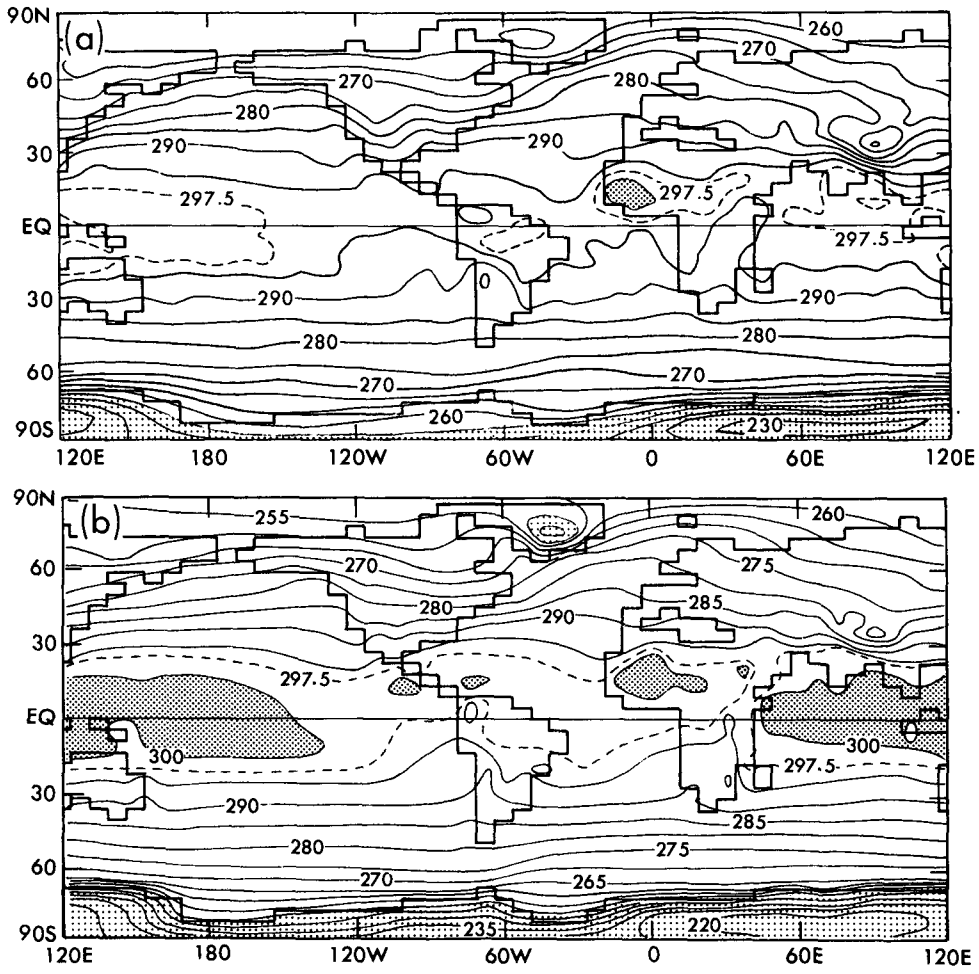

FIG. 5. Geographical distribution of annual mean surface air temperature (K). (a) The simulated distribution of the temperature averaged over the 100-year period of the S integration of the coupled model. (b) The observed distribution from Crutcher and Meserve (1970) and Taljaard et al. (1969). (The surface air temperature of the model is the temperature at the lowest finite difference level located at about 70 m above the surface.)

model, a preliminary integration of the AM model was performed over a period of 30 years starting from the initial condition of an isothermal atmosphere at rest. Throughout the course of this preliminary integration, sea surface temperature and sea-ice thickness are artificially maintained at observed climatological values. After the integration of the AM model over several years, the state of the model atmosphere exhibited no systematic trend. The sources or sinks of heat, which are required to maintain realistic temperature and sea-ice thickness in the mixed-layer ocean, are averaged over 10 annual cycles between the 20th and 30th years of this integration. In all three integrations described below, the seasonally and geographically varying heat flux is prescribed at the bottom of the mixed-layer ocean such that it is equivalent with the heat source (or sink) computed here.

c. *Standard integrations*

Starting from the state reached at the end of the preliminary integration, the AM model was integrated over the period of 40 years, allowing both the temperature and ice thickness of the mixed-layer ocean to change thermodynamically. The heat flux, which was determined from the preliminary integration, was prescribed at the bottom of the mixed layer as a function of season and geography. Owing to this heat flux, no systematic drift of the model climate was indicated, and the sea surface temperature and sea-ice thickness did not deviate significantly from the observed climatology.

d. *Computations of equilibrium responses*

In addition to the standard integration with the normal concentration of atmospheric carbon dioxide, two additional integrations were performed over the period of 40 years assuming twice and half the normal CO_2 concentration. The heat flux, which is prescribed at the bottom of the mixed layer in these two integrations, is identical to the flux prescribed in the standard integration. Toward the end of each integration the climate of the AM model is close to the state of equilibrium and exhibits very little trend. The quasi-equilibrium climates were computed for the cases of twice and half the normal CO_2 concentrations by computing the average states of the model over the last 10 annual cycles of the two integrations. For convenience of identification, these two quasi-equilibria are called E2X and EX/2, respectively. The quasi-equilibrium climate, obtained from the last 10 annual cycles of the standard integration, will be identified as ES. By subtracting the ES from the E2X and the ES from the EX/2, the equilibrium responses to the doubling and halving of atmospheric carbon dioxide were evaluated.

The equilibrium response of the AM model to the doubling (or halving) of atmospheric carbon dioxide can be compared with the transient response of the coupled ocean–atmosphere model at the time of CO_2 doubling (or halving). Since the delay due to the effective thermal inertia of the oceans is not permitted in the equilibrium response, the difference between the two responses indicates how oceans help in delaying the transient response of climate to increasing (or decreasing) concentration of atmospheric carbon dioxide. Although the oceanic uptake of heat changes throughout the transient response of the coupled ocean–atmosphere model, the heat flux at the bottom of the mixed-layer ocean does not change in the equilibrium response of the AM model. Thus, the comparison between the two responses should reveal how the oceanic uptake of heat alters the transient response of climate.

5. Simulated climate

The temporal variation of area-averaged, annual-mean, surface air temperature of the coupled ocean–atmosphere model during the 100-year period of the standard integration (S) is illustrated in Fig. 2. Similar time series of global-mean surface air temperature was obtained by Hansen et al. (1988) from their atmosphere–mixed-layer ocean model. This figure indicates

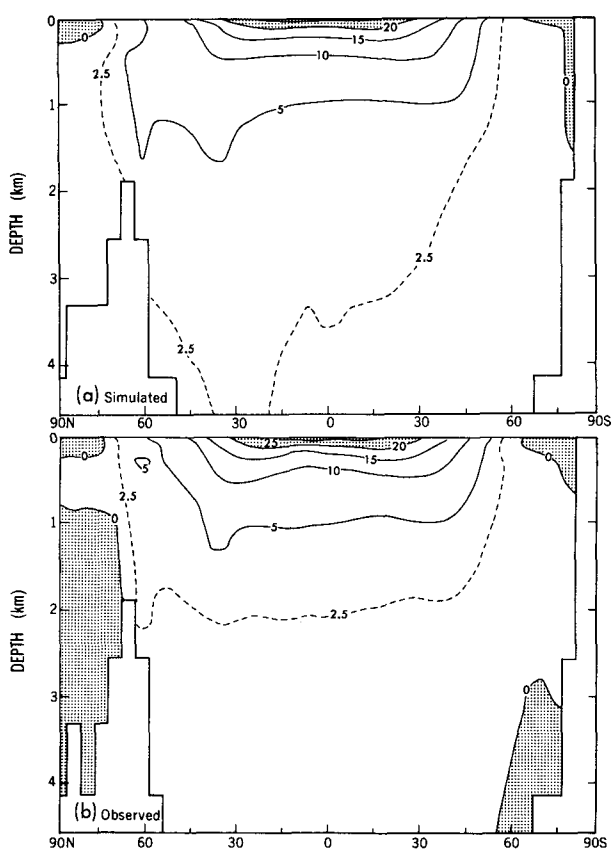

FIG. 6. Zonal-mean oceanic temperature (°C). (a) The simulated distribution averaged over the 100-year period of the S integration of the coupled model. (b) The observed annual-mean distribution from Levitus (1982).

that the global-mean and hemispheric-mean temperatures undergo interannual and interdecadal fluctuations of several tenths of a degree celsius. However, they appear to have no systematic trend, indicating that the initial condition for this S integration is close to the state of equilibrium. Although a very slow drift of the deep water temperature exists in some regions, such as the northern North Atlantic, the drift of global mean temperature at the depth of 4 km is about −0.1°C/100 years and is very small compared with the observed secular change in the North Atlantic (Roemmich and Wunsch 1984).

The geographical distributions of sea surface temperature and surface salinity averaged over the entire 100-year period of the S integration are compared with observations in Figs. 3 and 4, respectively. Although the adjustment of surface fluxes of heat and water described in section 3b is independent of the temporal variation of the oceanic surface, both temperature and salinity at the surface of the model oceans do not deviate substantially from the observed values during the course of the S integration as manifested in this figure.

Figure 5 compares the geographical distribution of

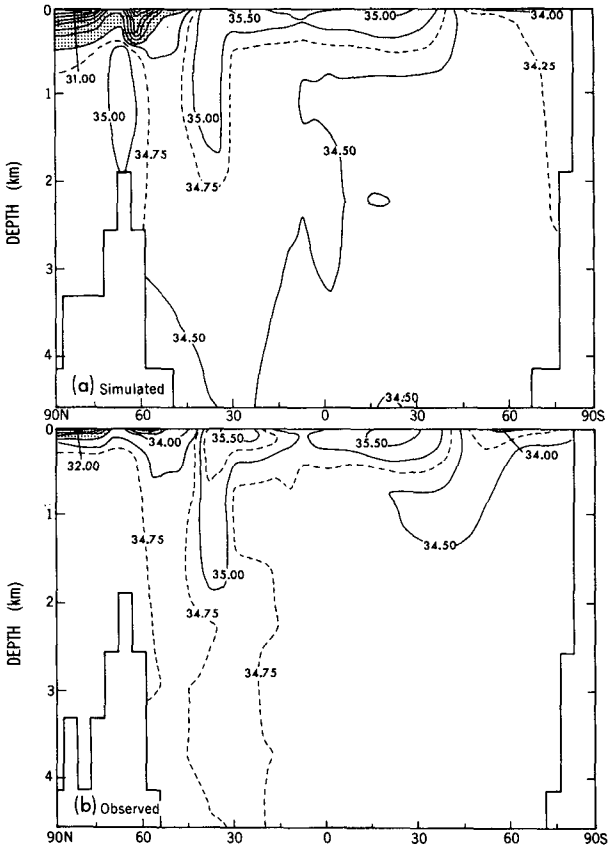

FIG. 7. Zonal-mean oceanic salinity (psu). (a) The simulated distribution averaged over the 100-year period of the S integration of the coupled model. (b) The observed distribution from Levitus (1982).

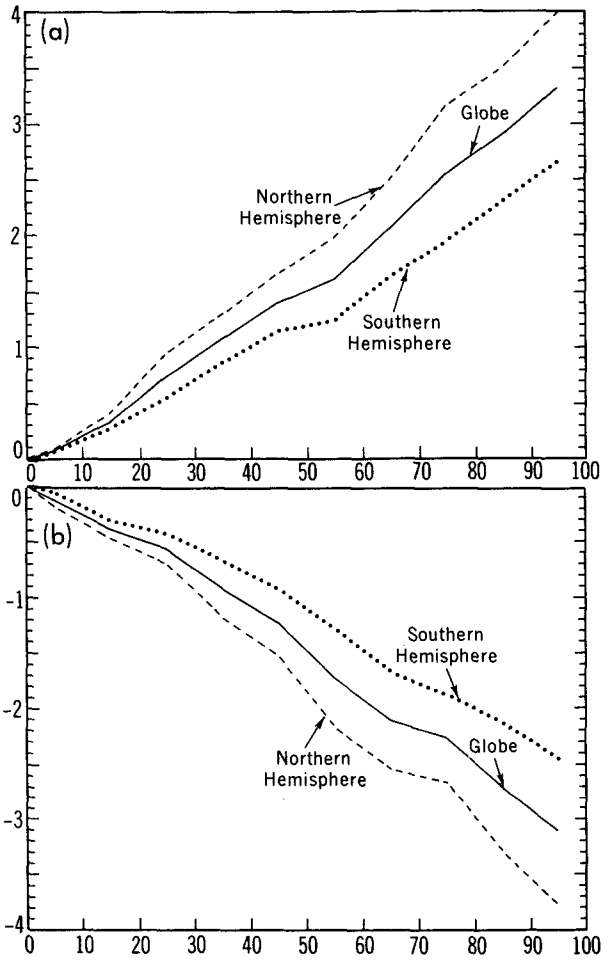

FIG. 8. The temporal variation of the differences in area-averaged, decadal-mean surface air temperature (°C) between the integrations (a) G and S, and (b) D and S. Solid, dashed, and dotted lines indicate the differences over the globe, and Northern and Southern Hemispheres, respectively.

the surface air temperature averaged over the 100-year period of the S integration with the observed distribution (Crutcher and Meserve 1970; Taljaard et al. 1969). This figure indicates that the surface air temperature in the model tropics is slightly, but systematically, lower than that observed due mainly to the exaggeration of the air–sea temperature difference by the model. In middle latitudes, the thermal ridges along the west coast of Europe and North America are reproduced very well. In general, surface air temperature over continents is simulated reasonably well, with the exception of the Antarctic continent where it is too high, partly because the model ice sheet has unrealistically low elevations due to the spectral filtering of topography.

The latitude–depth distribution of the zonal-mean temperature in the model ocean averaged over the 100-year period of the S integration is shown in Fig. 6 and is compared with the corresponding distribution of the

observed zonal-mean temperature compiled by Levitus (1982). Although the deep-water temperature is too warm by 1°–2°C, the general characteristics of zonal-mean subsurface temperature are well reproduced. For example, the 5° and 10°C isotherms are placed at depths of about 1 and 0.5 km, respectively. The success in reproducing the observed depth of the thermocline increases the likelihood that the CO_2-induced penetration of the thermal anomaly into the thermocline may be modeled realistically.

In Fig. 7, the latitude–depth distribution of zonal-mean salinity in the model ocean is also compared with the observed salinity compiled by Levitus (1982). Again, the model reproduces the observed characteristics of zonal-mean salinity in middle and low latitudes reasonably well. The model has an intense halocline in the Arctic and a much weaker halocline in the vicinity of the Antarctic continent, in qualitative agreement with the observed features. The simulated salinity of deep water, however, is too fresh, obscuring the northward intrusion of intermediate water in the Circumpolar Ocean of the Southern Hemisphere.

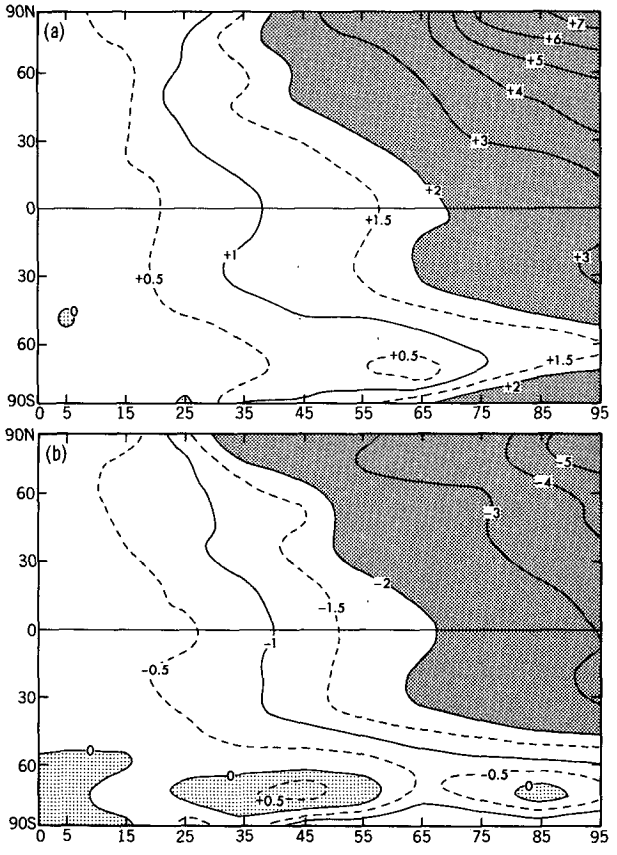

FIG. 9. The temporal variations of the differences in zonally averaged, decadal-mean surface air temperature (°C) between integrations (a) G and S, and (b) D and S.

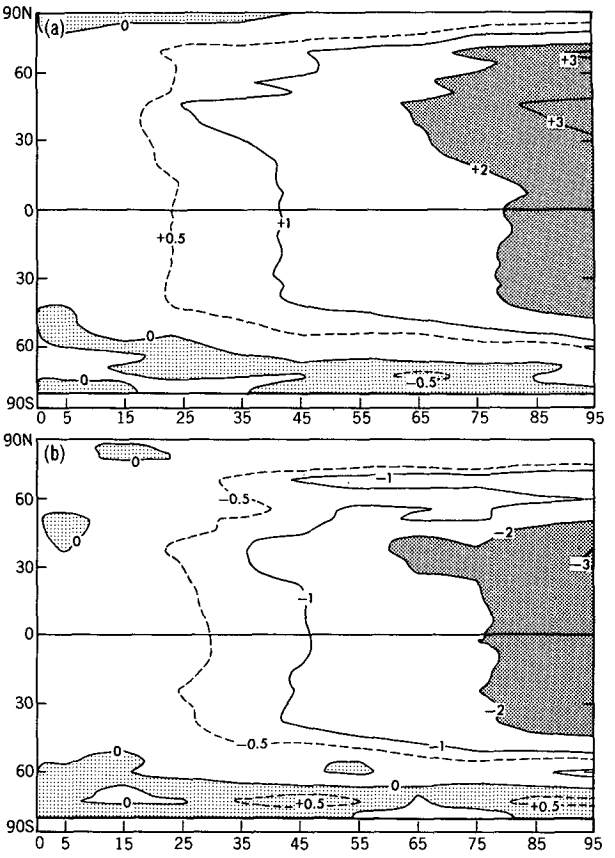

FIG. 10. Temporal variations of the difference in zonally averaged, decadal-mean sea surface temperature (°C) between the integrations (a) G and S, and (b) D and S.

6. Temperature response

The time-dependent response of the thermal structure of the coupled model to a gradual increase of atmospheric carbon dioxide is evaluated by subtracting a decadal mean state of the S integration from its corresponding decadal mean state of the G integration. To evaluate the response to a gradual reduction of carbon dioxide, a similar subtraction is made for each decadal mean state of the D integration. These subtractions are made to remove the climatic drift of the model, which results from the imbalance of initial conditions. Figure 8 shows that the global-mean and hemispheric-mean surface air temperatures increase or decrease depending upon whether the atmospheric CO_2 concentration increases or decreases. It is notable that the temperature response to a linear change of a CO_2 thermal forcing, after a brief initial phase of slower change, is close to being linear in time. [Note that an exponential increase (reduction) of atmospheric CO_2 concentration assumed here constitutes a linear increase (reduction) of thermal forcing]. This figure also indicates that the magnitude of the response averaged

over the Southern Hemisphere is substantially smaller than that of the Northern Hemisphere in both warming and cooling cases.

Figure 9 illustrates the time-dependent responses of the zonally averaged, decadal-mean surface air temperature to the gradual increase and reduction of atmospheric carbon dioxide. For the convenience of comparison, the shading convention is reversed between the two responses such that the pair of responses would look similar when they are antisymmetric to each other. In both experiments, the response of the zonal-mean surface air temperature increases in the Northern Hemisphere with increasing latitudes and is at a minimum at the equator. In the Southern Hemisphere the magnitude of the response in both cases increases from the equator to 30°S and then decreases to 70°S. The response becomes small and close to zero in the Circumpolar Ocean. It appears highly significant that, disregarding the reversal of sign, the latitudinal profiles of the response to the gradually increasing and decreasing atmospheric carbon dioxide are qualitatively similar to each other. A similar latitudinal profile was also obtained by Bryan et al. (1988) and Manabe et al. (1990) in the zonal-mean responses of surface air temperature of their models with the sector and global computational domain, respectively.

The time-dependent responses of zonally averaged, decadal-mean sea surface temperature to a gradual increase and decrease of atmospheric carbon dioxide are illustrated in Fig. 10. Again, the two responses are of opposite sign. They are at a local minimum around the equator and increase with increasing latitudes up to 40° in both hemispheres. In contrast to the surface air temperature in the previous figure, sea surface temperature has a more symmetric response with respect to the equator. Ice formation does not allow polar amplification to take place in the surface temperature of the Northern Hemisphere oceans.

The temporal variations of zonally averaged, decadal-mean thickness of sea ice from the G, S, and D integrations are illustrated in Fig. 11. In the G integration, in which the atmospheric CO_2 concentration is increased with time, the thickness of sea ice over the Arctic Ocean is reduced markedly from 3 m to less than 1 m during the 100-year period. Owing to the reduction of sea ice, the exchange of heat between the oceanic water surface and overlying air increases, resulting in the large increase of surface air temperature over the Arctic Ocean. It is surprising, however, that the sea-ice thickness in the G integration increases significantly in the immediate vicinity of the Antarctic Continent despite the increase of atmospheric carbon dioxide. This is consistent with the slight reduction of sea surface temperature mentioned earlier (Fig. 10a). It will be shown in section 9a that, owing to the intensification of the near-surface halocline caused by the increased supply of water at the oceanic surface, the convective mixing of cold near-surface water with warmer, underlying water becomes less frequent, resulting in the increase of sea ice and slight reduction of sea surface temperature. In the D integration, in which the atmospheric concentration of carbon dioxide is decreased with time, the thickness of sea ice increases dramatically over the Arctic Ocean, but is reduced slightly in the immediate vicinity of the Antarctic Continent. These changes of sea ice are opposite in sign from those of the G integration because the process involved is reversed as discussed in section 9a.

As explained in sections 1 and 3, the time-dependent response of the coupled ocean–atmosphere model to a gradual change of atmospheric carbon dioxide is compared to the equilibrium response of the atmosphere–mixed-layer ocean model to a doubling (halving) of carbon dioxide. Figure 12a illustrates the geographical distribution of the time-dependent response of surface air temperature of the coupled ocean–atmosphere model to the gradual increase of atmospheric carbon dioxide. The distribution represents the response averaged from the 60th to the 80th years, when the CO_2 concentration in the model atmosphere is approximately doubled. For comparison, the equilibrium response of surface air temperature of the atmosphere–mixed-layer ocean model to a doubling of atmospheric carbon dioxide is shown in Fig. 12b. The ratio of the transient to equilibrium response is shown in Fig. 12c.

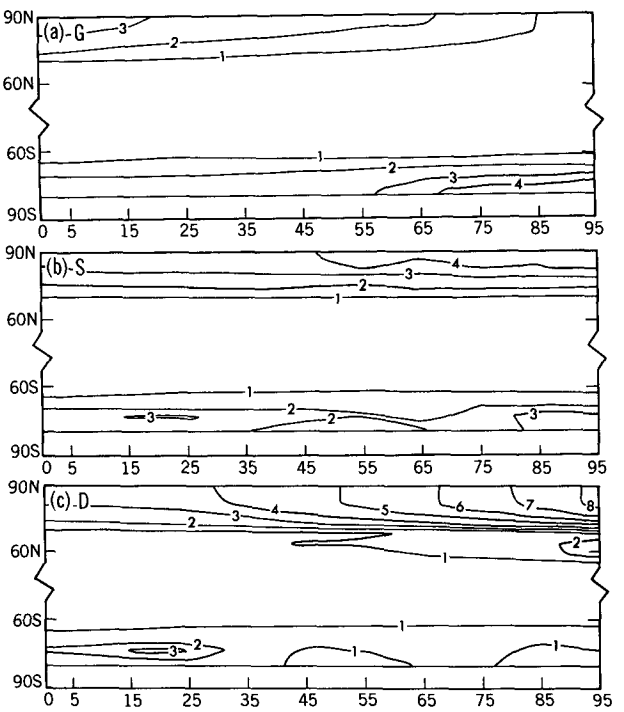

FIG. 11. The temporal variations of zonally averaged, decadal-mean thickness of sea ice (meters) from the integrations (a) G, (b) S, and (c) D.

Figure 12a indicates that the transient response of surface air temperature is particularly slow over the northern North Atlantic and the Circumpolar Ocean of the Southern Hemisphere, where the deep vertical mixing of water predominates and the effective oceanic thermal inertia is very large, as discussed later. On the

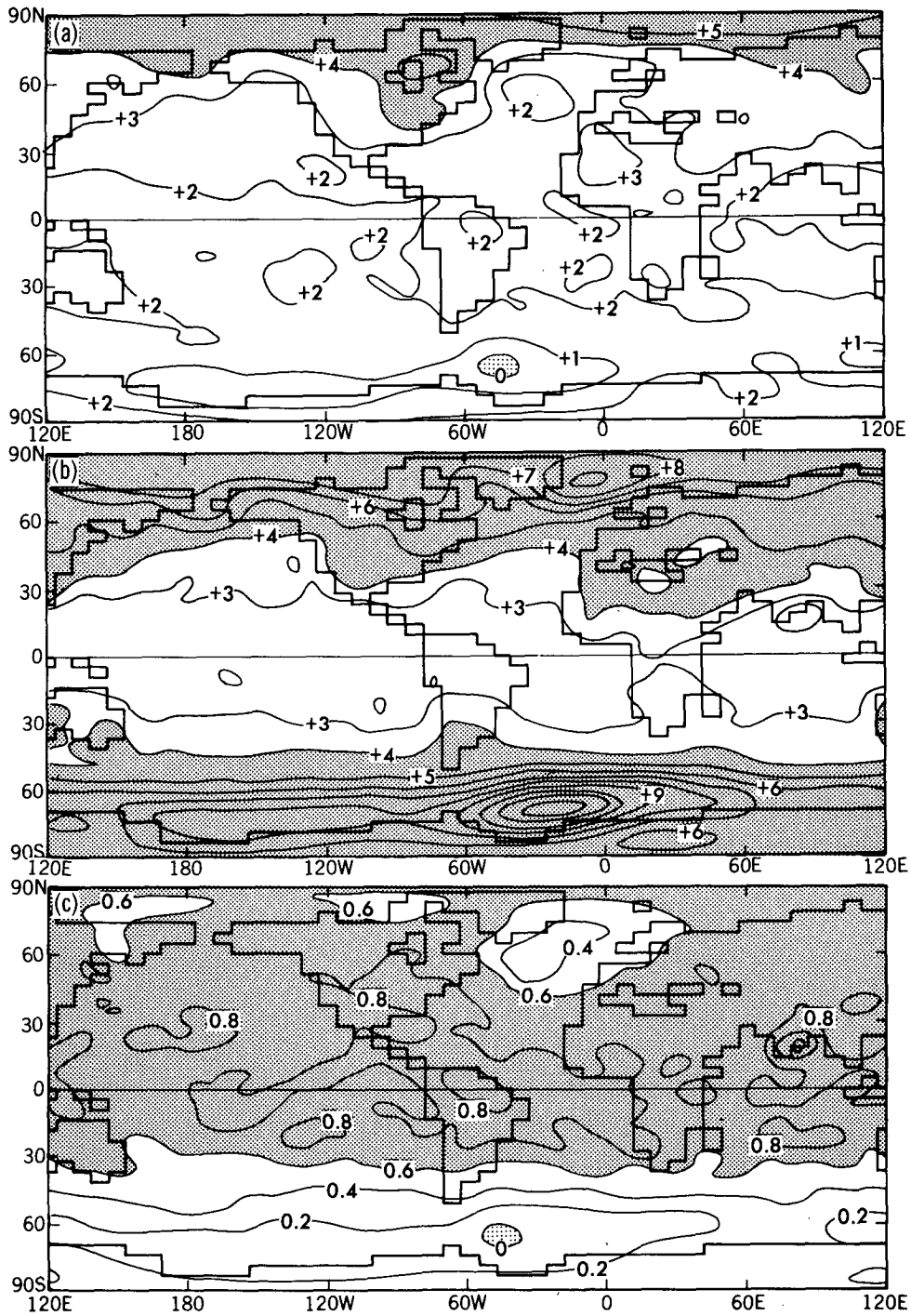

FIG. 12. (a) The transient response of the surface air temperature of the coupled ocean–atmosphere model to the 1%/year increase of atmospheric carbon dioxide. The response (°C) is the difference between the 20-year (60th to 80th year) mean surface air temperature from the G integration and 100-year mean temperature from the S integration. (b) The equilibrium response of surface air temperature to the doubling of atmospheric carbon dioxide. The response is the difference between the two 10-year mean states of the E2X and ES integrations. (c) The ratio of the transient to equilibrium responses.

other hand, the equilibrium response of surface air temperature shows polar amplification in both hemispheres. The equilibrium response is particularly large along the coast of the Antarctic Continent, enhanced by the poleward retreat of sea ice with high surface albedo. Thus, the ratio of the transient to equilibrium response of surface air temperature falls below 0.4 in the northern North Atlantic and is near zero in the Circumpolar Ocean of the Southern Hemisphere.

In middle latitudes of the Northern Hemisphere, the

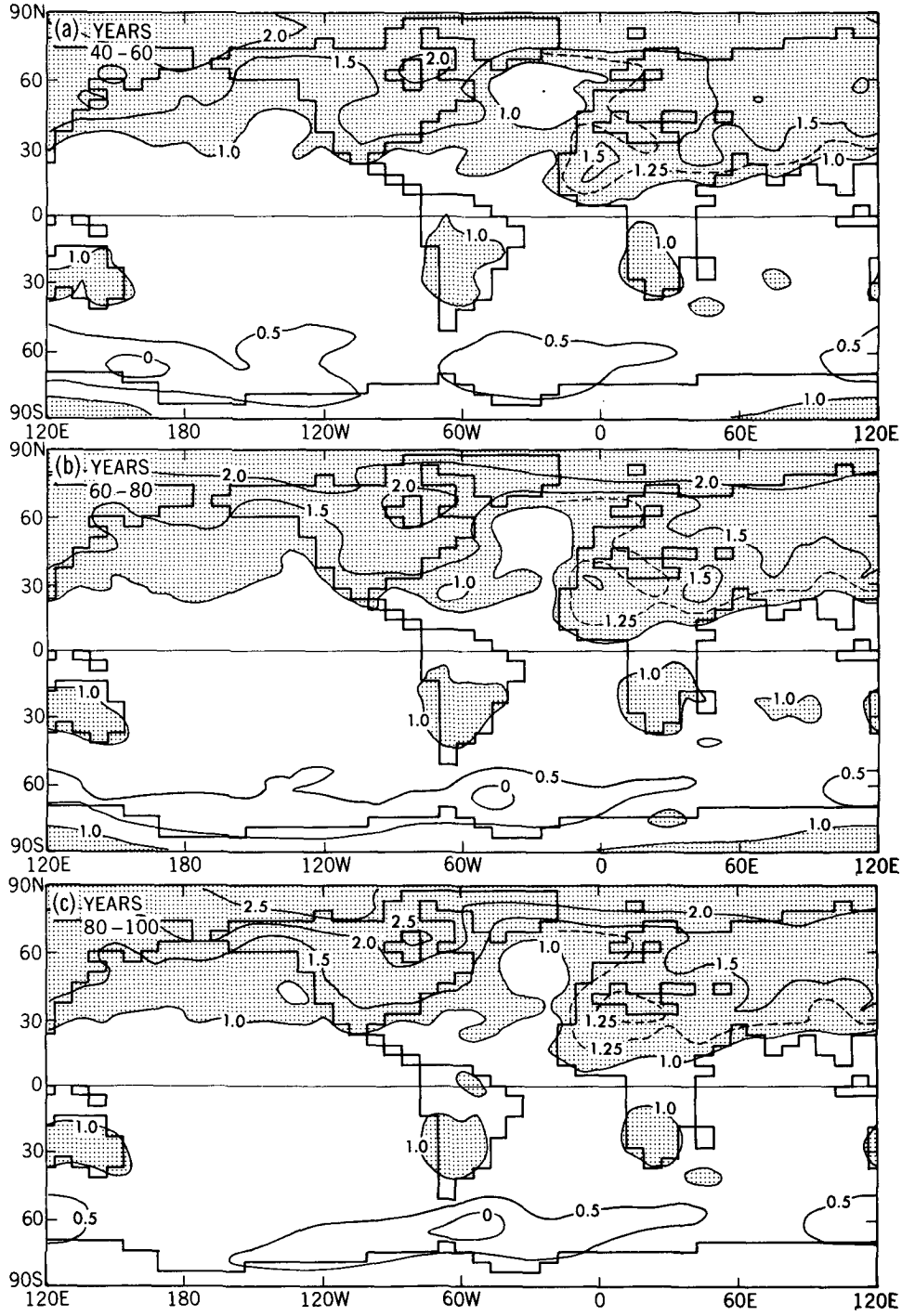

FIG. 13. The geographical distributions of the differences of 20-year mean surface air temperature between the G and S integrations as normalized by their global mean values which are 1.54°, 2.31°, and 3.01°C for the 40th–60th year (a), 60th–80th year (b), and 80th–100th year (c) periods, respectively.

increase of surface air temperature in response to a gradual increase of atmospheric carbon dioxide tends to be larger over continents than oceans. Although it is tempting to speculate that the smaller oceanic warming in the time-dependent response may be mainly attributable to the delay caused by the large effective thermal inertia of the oceans, one should note that a similar land–sea contrast in warming is also in-

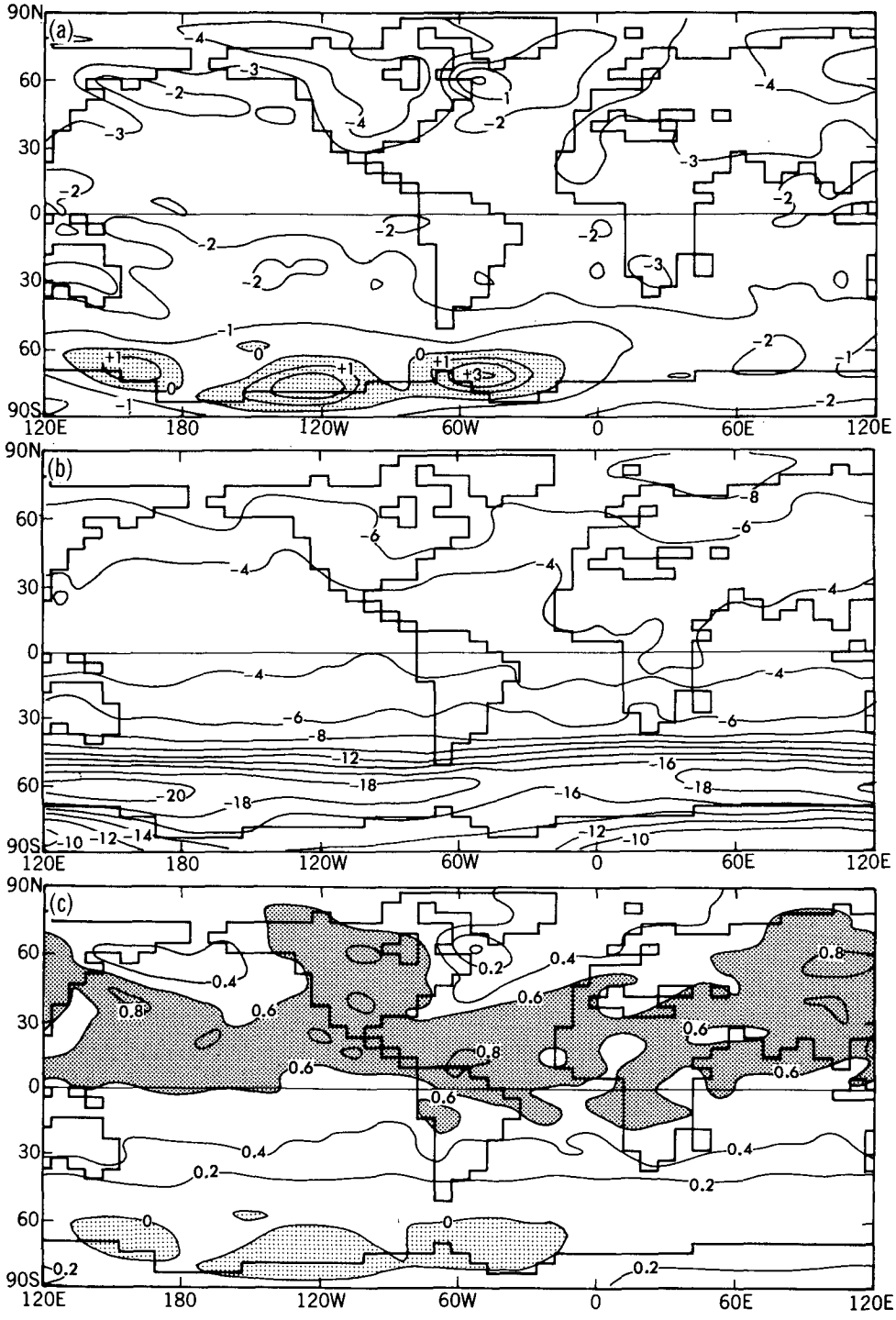

FIG. 14. Same as Fig. 12, except that it illustrates the change of surface air temperature from the CO_2 reduction experiments. (a) Transient response to the 1%/year reduction of atmospheric CO_2. (b) Equilibrium response to the CO_2 halving. (c) The ratio of transient to equilibrium response.

dicated in the equilibrium response of surface air temperature shown in Fig. 12b. In fact, the ratio of the transient to the equilibrium responses of surface air temperature in middle latitudes of the Northern Hemisphere does not vary substantially from continental to oceanic regions, with the exception of the northern North Atlantic where the ratio is particularly small as described above. It will be shown in section 7a that the relatively small warming over oceans in middle latitudes in both transient and equilibrium responses is attributable partly to a larger increase in the efficiency of evaporative heat loss from the wet oceanic surface as compared with the continental surface.

To evaluate how the geographical distribution of surface air temperature change evolves in the CO_2 growth experiment, the differences in surface air temperature averaged over the 40th–60th, 60th–80th and 80th–100th year periods are normalized by their respective global mean values and are shown in Fig. 13. In the shaded regions, where the normalized difference is larger than one, the CO_2-induced warming is larger than its global average. This figure indicates that many of the features of the temperature change described in the preceding paragraphs are shared by the patterns from the three 20-year periods. Although the maps from all 20-year periods are not shown here, the geographical distribution of surface air temperature change is approximately self-similar during the course of the experiment, except the first 20-year period when the natural variation of surface air temperature overshadows the CO_2-induced change.

It is of interest to examine how the response of surface air temperature described above compares with the results from the companion cooling experiment. Figure 14 contains a set of three pictures, which is the companion set of Fig. 12, and illustrates the transient and equilibrium responses, and the ratio of the former to the latter. As expected, the geographical distribution of the response of surface air temperature has a similar distribution but reverses sign from the CO_2 growth experiment described above. Again, the transient response is much smaller than the equilibrium response over the northern North Atlantic and the Circumpolar Ocean of the Southern Hemisphere, as indicated by the small ratios in Fig. 14c. It is of interest that an area of relatively small ratio also appears near the Aleutian Archipelago of the North Pacific.

Qualitatively, the ratio of transient to equilibrium response of surface air temperature discussed above is significantly different between the CO_2 growth and CO_2 reduction experiments. For example, comparing Figs. 12c and 14c, one notes that the regions of low ratio in high-latitude oceans are much more extensive in the CO_2 reduction than the growth experiment. To quantify more clearly this difference, both transient and equilibrium responses of surface air temperature are area averaged and are tabulated in Table 1 together with this ratio. According to this table, the equilibrium

TABLE 1. Area-mean responses of surface air temperature (°C) to a doubling and halving of atmospheric CO_2. The transient response represents an average over the 20-year period between the 60th and 80th years of each experiment. The responses are averaged over the Northern Hemisphere (NH), Southern Hemisphere (SH), or the entire globe (G).

(a) CO_2 Growth Experiment

	Transient response (G-S)	Equilibrium response E2X-ES	Ratio (G-S): E2X-ES
NH	2.76	3.89	.710
SH	1.86	4.04	.460
G	2.31	3.97	.582

(b) CO_2 Reduction Experiment

	Transient response (D-S)	Equilibrium response EX/2-ES	Ratio (D-S): EX/2-ES
NH	−2.68	−4.54	.590
SH	−1.70	−8.71	.195
G	−2.19	−6.23	.352

response of surface air temperature to the halving of atmospheric carbon dioxide is substantially larger than that of doubling CO_2. This is because the sensitivity of equilibrium surface air temperature depends critically upon the value of the surface air temperature itself. As the temperature of the model atmosphere decreases, snow and sea ice occupy wider areas, exerting a stronger positive feedback effect upon climate and enhancing its sensitivity (Spelman and Manabe 1984). This table also indicates that the transient response of surface air temperature to the halving of atmospheric carbon dioxide is similar in magnitude to the corresponding response to the doubling. Thus, the ratio of transient to equilibrium response is significantly smaller in the CO_2 reduction experiment than the CO_2 growth experiment, particularly in the Southern Hemisphere. As discussed below, this is attributable to the difference in the effective thermal inertia of the model oceans between the two experiments. Although the transient response of surface air temperature in the CO_2 reduction experiment is enhanced by the stronger albedo feedback effect of snow and sea ice, it is reduced due to the deeper penetration of heat into the oceans and becomes similar in magnitude to the corresponding response in the CO_2 growth experiment.

The geographical distribution of the time-dependent response of sea surface temperature of the coupled ocean–atmosphere model is time averaged over the 60th to 80th year period and is illustrated in Fig. 15. The responses to the gradual increase and decrease of CO_2 are shown in the upper and lower half of the figure, respectively. The response of sea surface temperature may be different from that of surface air temperature in high latitudes where sea ice separates air from underlying water. Over the Arctic Ocean, for example, the sea surface temperature hardly changes because the

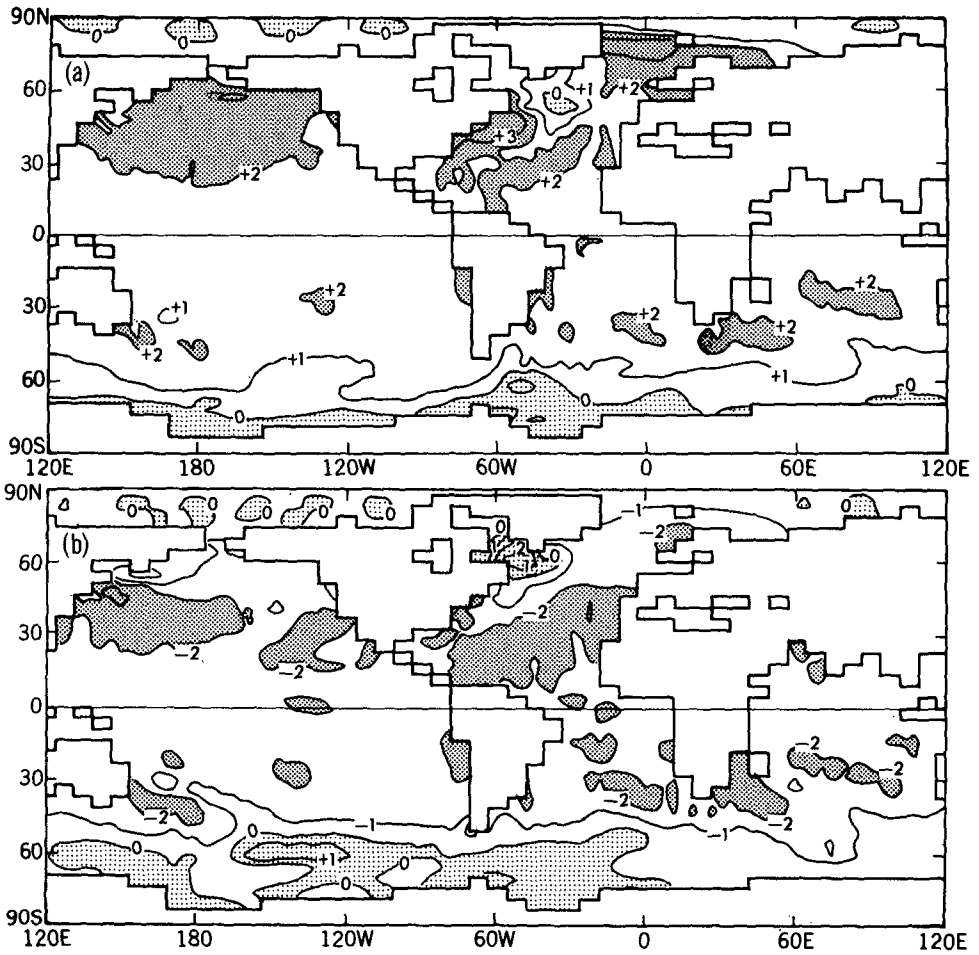

FIG. 15. The geographical distribution of the sea surface temperature difference (°C) between the G and S integrations (a) and the D and S integrations (b). The sea surface temperature is time averaged over the 60th to 80th year period of each integration.

heat involved in melting or freezing sea ice prevents it from deviating significantly from the freezing point. This is in sharp contrast to the large change of surface air temperature, which results from the change in heat supply from underlying water due to the large change in the thickness of sea ice.

In those oceanic regions of high latitudes where the vertical mixing of heat penetrates very deeply, both surface air temperature and sea surface temperature hardly change. For example, the change of sea surface temperature is small over the Circumpolar Ocean of the Southern Hemisphere. It even has an opposite sign in some parts of the Weddell and Ross seas. In both the G and D integrations, the change of sea surface temperature is small to the south of Greenland where the change of surface air temperature is small. It is notable that the change of sea surface temperature is also small over the Okhotsk Sea in the D integration.

So far, the time-dependent response of temperature near the atmosphere–ocean interface of the coupled model has been described. To examine the response of temperature in the free atmosphere and subsurface ocean layers, Fig. 16 is constructed. It illustrates, as a function of latitude and height (or depth), the responses of zonal-mean temperature averaged over the 60th to 80th years of the CO_2 growth and reduction experiments. In general, the gradual increase and decrease of atmospheric carbon dioxide induces time-dependent responses opposite in sign but qualitatively similar in distribution. In both responses, the change of atmospheric temperature is very large in the polar region of the Northern Hemisphere but confined to the near-surface layer. On the other hand, it is very small in the near-surface layer over the Antarctic Continent and its surroundings. The interhemispheric asymmetry in the response to the model atmosphere decreases with increasing altitude and becomes much less evident in the mid troposphere.

In the model oceans, the anomalies of zonal-mean temperature penetrate into deep levels around 70°N

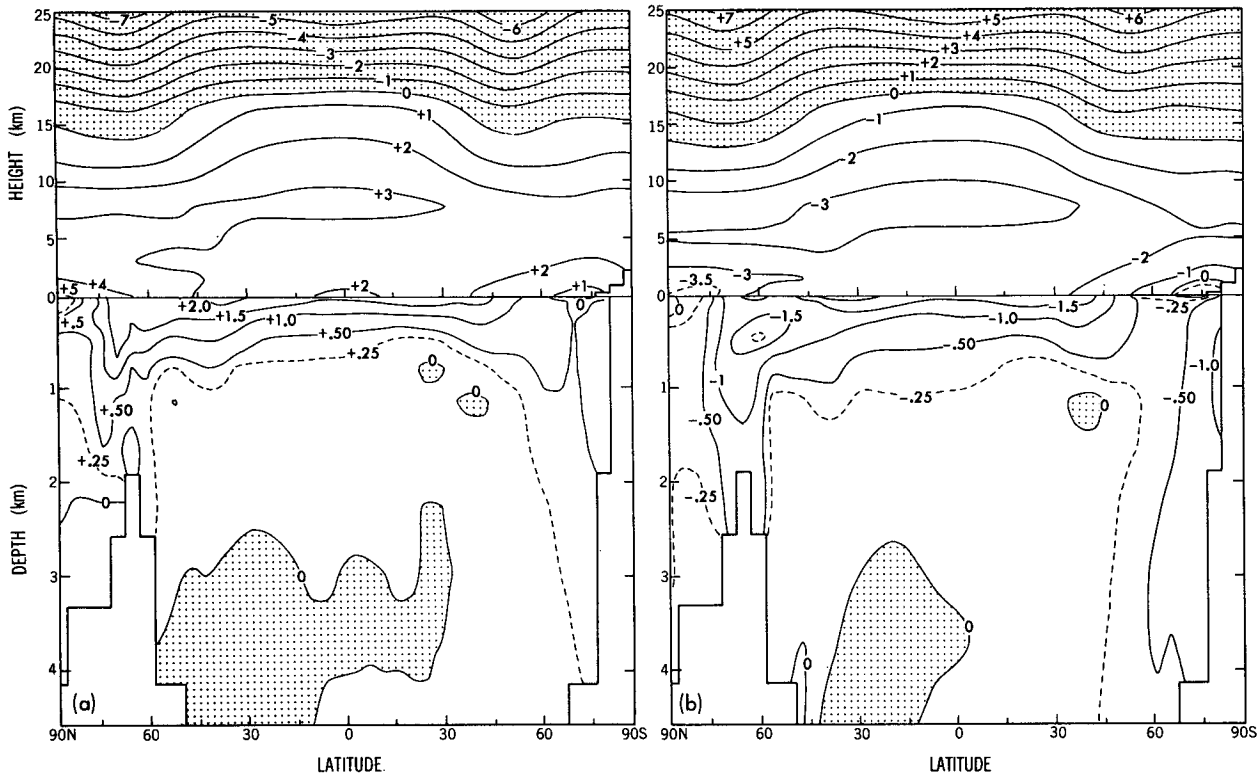

FIG. 16. The latitude–depth (or height) distribution of the difference in zonal-mean temperature (°C) between (a) the G and S and (b) the D and S integrations. The temperature is obtained by taking an average over the 60th–80th year period of each integration.

in the Northern Hemisphere and in the Circumpolar Ocean of the Southern Hemisphere. On the other hand, the anomalies are limited to the upper layer of the model oceans in low latitudes.

The vertical spreading of positive and negative anomalies of oceanic temperature are evaluated by computing the effective depth of positive and negative anomalies in the G and D integrations, respectively. For example, the effective depth of the positive anomaly d_+ is defined for the CO_2 increase experiment by use of the following formula:

$$d_+ = \left(\int_0^{Z_b} (-Z)\,\delta_+ T dZ\right) \Big/ \left(\int_0^{Z_b} \delta_+ T dZ\right),$$

where depth Z is negative downward, zero at the oceanic surface, and Z_b at the bottom of the sea. $\delta_+ T$ is the positive difference in oceanic temperature between the G and S integrations. If the difference is negative, it is set equal to zero. For the D integration, the effective depth of negative anomaly d_- is defined in a similar manner, except that $(\delta_+ T)$ is replaced by the negative anomaly $(\delta_- T)$.

By use of these formulas, the geographical distributions of d_+ and d_- are computed for both CO_2 growth and reduction experiments and are illustrated in Fig. 17. This figure clearly indicates that the penetration depths of both positive and negative temperature anomalies are particularly large in the Circumpolar Ocean of the Southern Hemisphere and the northern North Atlantic where the time-dependent response of sea surface temperature is small. This is because the CO_2-induced changes in oceanic heat storage are spread over very deep columns of water in these areas.

When one compares the penetration depth of the positive anomaly with that of the negative anomaly shown in Fig. 17, one notes that the latter is usually larger, particularly in high latitudes. As discussed in sections 8 and 9, this difference in penetration depth is attributable to opposing changes in the static stability of the upper layer of the model ocean. Because of the difference in the penetration depth of the thermal anomaly, the effective thermal inertia of the oceans is much larger in the CO_2 reduction than in the CO_2 growth experiment, accounting for the smaller transient to equilibrium ratio in the former case.

7. Heat balance

a. *Surface heat balance*

In section 6, it was noted that in middle latitudes, both the equilibrium and the transient responses of surface air temperature are significantly larger over continents than over the oceans. To explore the mechanisms responsible for the land–sea contrast in surface

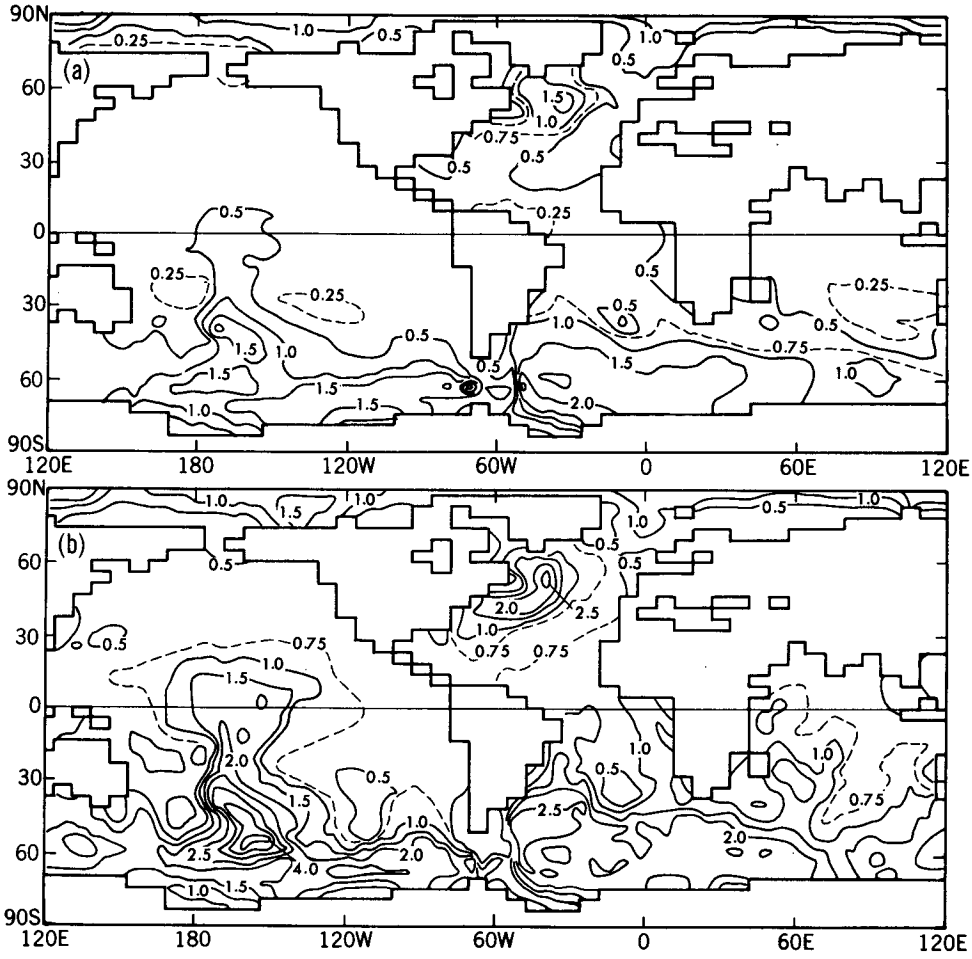

FIG. 17. The geographical distributions of penetration depth of (a) the positive anomaly of oceanic temperature in the CO_2 growth experiment and (b) the negative anomaly of temperature in the CO_2 reduction experiment. See the main text for the definition of positive and negative anomalies. Units are in kilometers.

air temperature change mentioned above, the CO_2-induced changes in various components of the surface heat budget are zonally averaged over oceans and continents separately and are illustrated as a function of latitude in Fig. 18. This was done for both the equilibrium response for CO_2 doubling and the time-dependent response to gradually increasing CO_2. For reference, zonally averaged heat budget components from the standard S integration are also shown in the upper portion of the figure. The responses of radiative fluxes are further subdivided into solar and terrestrial components and are shown in Fig. 19 for both oceans and continents. In both Figs. 18 and 19, a flux has a positive sign if it represents surface heat gain, but has a negative sign if it represents surface heat loss.

These figures indicate that the land–sea contrast in equilibrium response of surface air temperature to the doubling of atmospheric carbon dioxide is partly attributable to the larger increase in the evaporative heat loss from the oceanic as compared with continental surfaces. Over the oceanic surface, saturation vapor pressure increases due to the sea surface temperature increase, thereby enhancing the evaporative heat loss. On the other hand, the change in evaporation is smaller over continents where the rate of evaporation from the soil surface is less than the potential rate because soil is often not saturated with water. This land–sea difference in the CO_2-induced change of evaporative heat loss contributes to the land–sea contrast in warming in the equilibrium response experiment.

Another relevant process is the positive feedback effect of snow cover. As Fig. 19d indicates, solar energy absorbed by continental surfaces increases significantly around 30°–50°N due to the poleward retreat of snow cover. Over the oceans, the surface absorption of solar energy increases due to the reduction of sea ice over the Arctic Ocean, but does not change significantly in middle latitudes. Both the increased evaporative heat loss over oceans and enhanced solar absorption over continents contribute to the land–sea contrast of

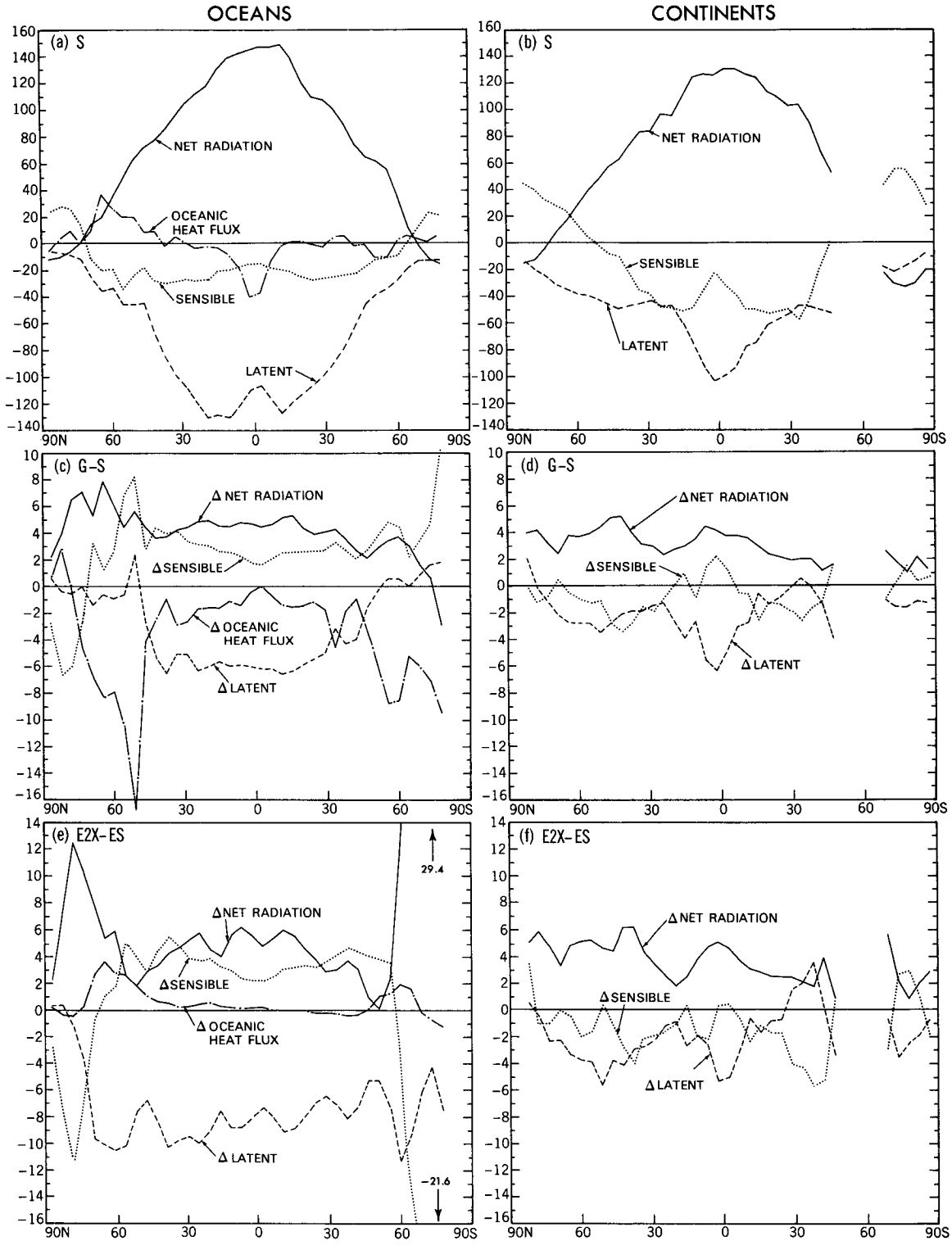

FIG. 18. Top: the latitudinal profile of zonal-mean surface heat balance components over oceans (a) and continents (b) averaged over the 60th to 80th year of the S integration. Middle: the latitudinal profiles of the zonal-mean difference in surface-heat balance components between the G and S integrations over oceans (c) and continents (d) averaged over the 60th to 80th year period. Bottom: the latitudinal profiles of the zonal-mean difference in surface heat balance components between the E2X and ES integrations over oceans (e) and continents (f). The solid, dashed, dotted, and dash-dotted lines indicate the surface values of net radiation, latent heat flux, sensible heat flux, and oceanic heat flux (or their differences), respectively. Positive (or negative) values indicate energy gain (or loss) for the surface. Units are W m^{-2}.

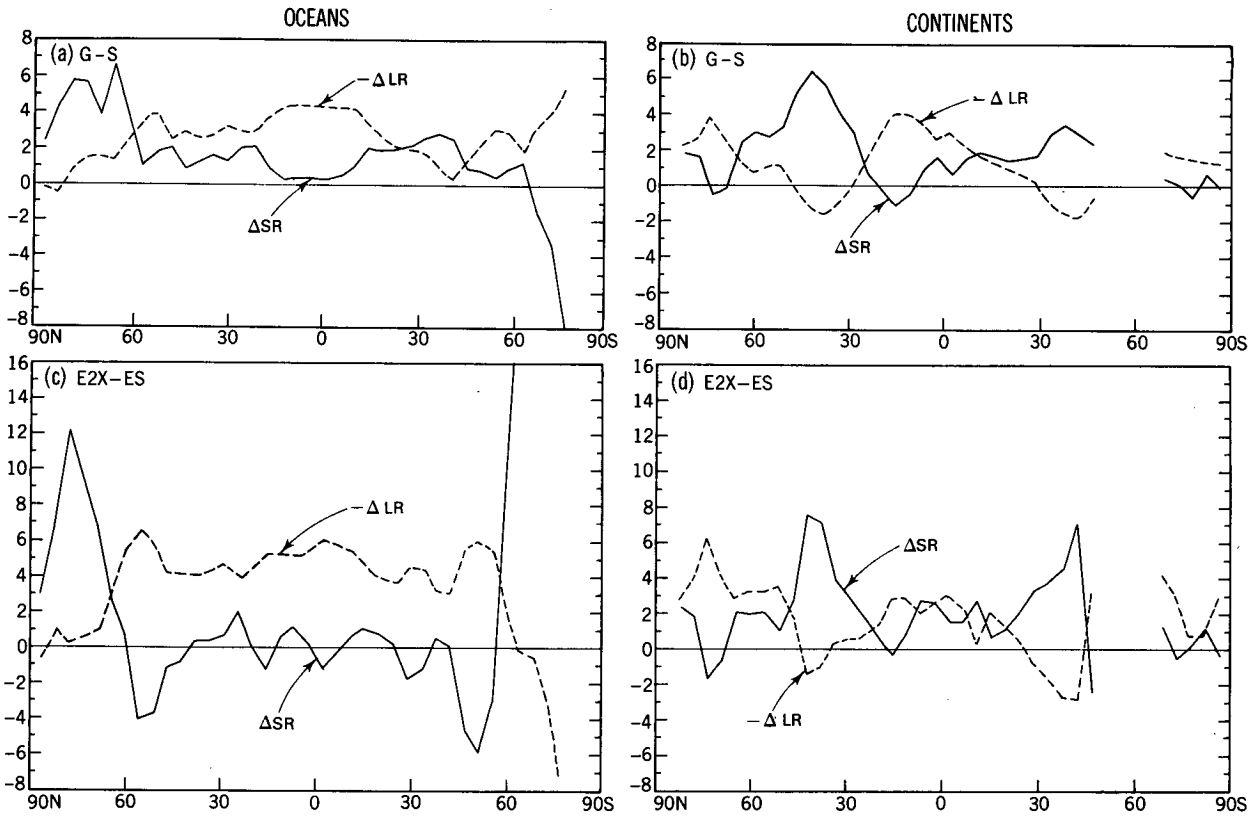

FIG. 19. Top: the latitudinal profiles of the zonal-mean differences in surface heat fluxes of solar and terrestrial radiation between the G and S integrations over oceans (a) and continents (b) averaged over the 60th to 80th year period. Bottom: the latitudinal profiles of the zonal-mean differences in surface heat fluxes of solar and terrestrial radiation between the E2X and ES integrations over oceans (c) and continents (d). The solid and dashed lines indicate the differences in solar and terrestrial fluxes, respectively. Positive values indicate energy gain for the surface. Units are W m^{-2}.

warming in middle latitudes. The larger warming of the continental surface, in turn, is responsible for the smaller net heat loss through the upward fluxes of sensible heat and terrestrial radiation, as indicated in Figs. 18 and 19.

With regard to the time-dependent response of the coupled ocean–atmosphere model, Fig. 18c illustrates the latitudinal profiles of the changes in various components of surface heat budget averaged over the 60th to 80th years when the atmospheric concentration of the CO_2 is doubled. This figure indicates that the CO_2-induced change of oceanic heat flux has a large negative contribution to the heat balance of the oceanic surface between 40° and 80°N. It implies that the supply of heat from the interior of the ocean to the surface is reduced markedly in this latitude belt. Over the northern North Atlantic, where the vertical mixing of water penetrates very deeply, the heat thus sequestered is spread over a very deep water column, preventing significant warming of the surface of the ocean (see section 9 for further discussion of this topic). Although this is the main reason why the sea surface temperature of the northern North Atlantic fails to increase significantly in the CO_2 growth experiment, there are other factors which make the warming of the oceanic surface smaller than that of the continental surface. For example, Fig. 18c indicates that, in middle and low latitudes, the increase in evaporative cooling of the oceanic surface is much more than the corresponding cooling of the continental surface, which is often not saturated with water. In addition, the heating due to the absorption of solar energy increases substantially over continents around 40°N, resulting from the poleward retreat of highly reflective snow cover (Fig. 19b). As was the case with the equilibrium response of the atmosphere–mixed-layer ocean model, both of these changes in the surface heat budget enhance the land–sea contrast of warming in middle and low latitudes.

b. Oceanic heat storage

To evaluate the CO_2-induced change in the heat budget of the model oceans, the latitudinal profiles of net surface heating and the rate of oceanic heat storage zonally averaged over the oceanic portion of a latitude belt are obtained from the G, D, and S integrations. The influence of the increase and reduction of atmospheric carbon dioxide is averaged over the entire 100-

year period and is illustrated in the upper and lower half of Fig. 20, respectively. In this figure, net surface heating represents the difference between the heating due to the surface absorption of radiative energy and cooling due to the upward fluxes of sensible and latent heat through the boundary layer. It is identical in magnitude but opposite in sign to the oceanic heat flux illustrated in Fig. 18.

Figure 20 indicates that, despite the horizontal uniformity of the change in concentration of atmospheric carbon dioxide, the change in net surface heat flux is highly variable with respect to latitude and is a maximum around 60°S and 55°N latitude. As explained below, these maxima in the change in net surface heat flux are attributable partly to the failure of sea surface temperature to rise significantly in the Circumpolar Ocean of the Southern Hemisphere and the northern North Atlantic.

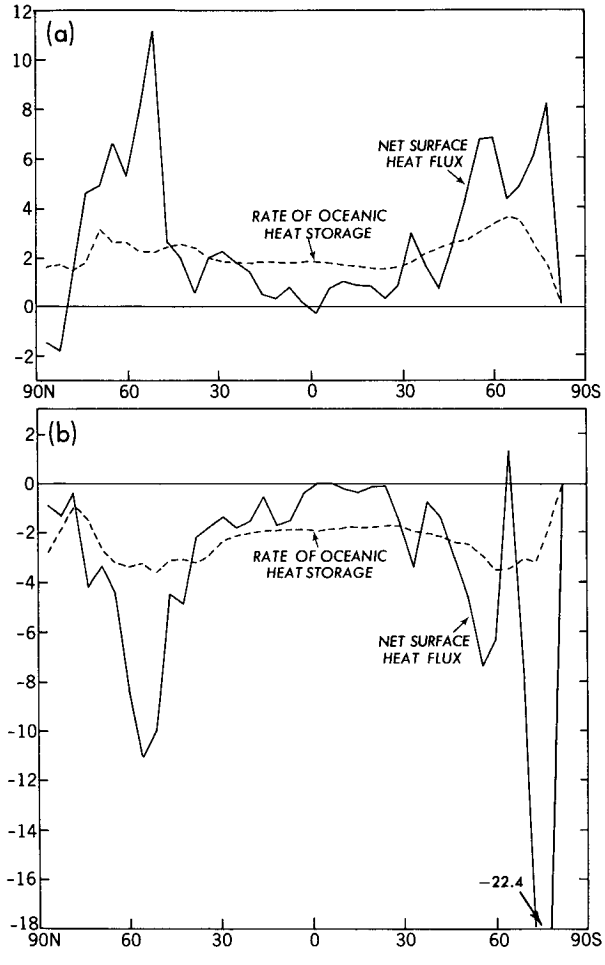

FIG. 20. The latitudinal profile of the zonal-mean differences of oceanic heat budget components between (a) the G and S integrations and (b) the D and S integrations. Solid line: the change in net oceanic surface-heat flux. Dashed line: the change in the rate of oceanic heat storage. These values represent the averages over the entire 100-year period of each experiment. Units are W m^{-2}. The change of heat storage attributable to sea ice is neglected.

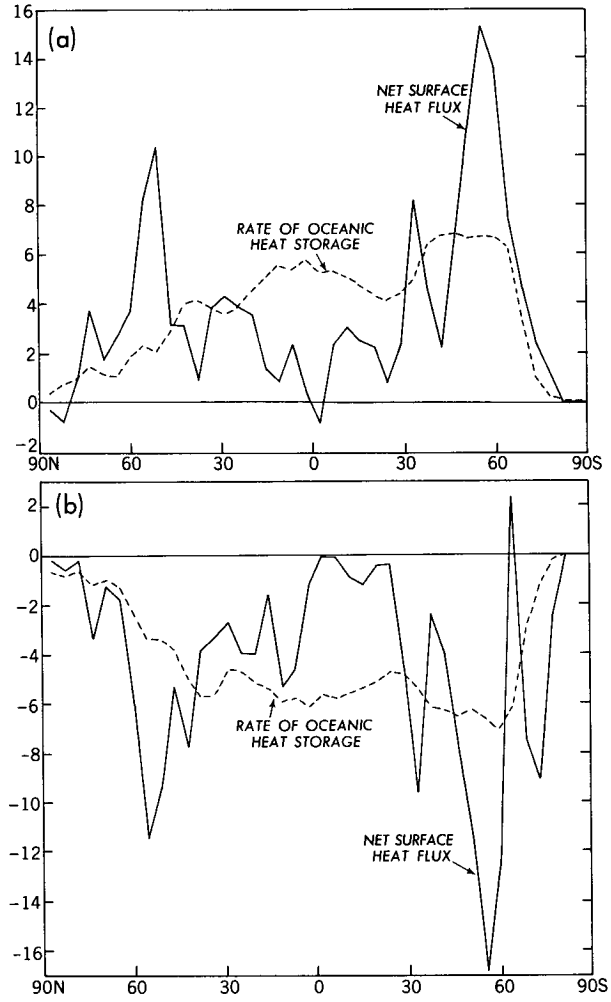

FIG. 21. Same as Fig. 20 except that the changes in both net oceanic surface heat flux (solid line) and the rate of heat storage (dashed line) are integrated over an entire latitude belt with the meridional span of 1 m. Units are 10^7 W m^{-1}.

In the CO_2 growth experiment, for example, both carbon dioxide and water vapor increase in the model atmosphere, thereby increasing the downward flux of terrestrial radiation, as shown in Figs. 18 and 19, and storing heat in the model oceans. Over the Circumpolar Ocean of the Southern Hemisphere and northern North Atlantic where the vertical mixing of water penetrates very deeply, the stored heat is spread over a deep water column, thereby reducing the warming of the sea surface. The absence of significant surface warming prevents the increase of heat loss from the oceanic surface through upward fluxes of sensible and latent heat, as well as terrestrial radiation (as Fig. 18c indicates), and contributes to the net heating of the oceans as indicated in Fig. 20.

In order to evaluate the CO_2-induced change in the heat budget over an entire latitude circle rather than a unit oceanic area, the two components of the heat

budget shown in Fig. 20 are multiplied by the longitudinal span of oceans at each latitude and are shown in Fig. 21. Focusing attention on the results from the CO_2 growth experiment shown in Fig. 21a, one notes that the CO_2-induced change of the heat budget exhibits a large interhemispheric asymmetry dominated by the Circumpolar Ocean of the Southern Hemisphere. Although the changes in both net surface heat flux and the rate of oceanic heat storage are at a maximum around 60°S, the former is much greater than the latter. On the other hand, the change in the net surface heat flux is less than the change in the net heat storage in low latitudes where the CO_2-induced increase in net oceanic heat flux is small due to the marked increase in evaporative heat loss from the surface. These results imply that the poleward heat transport by ocean currents is reduced in the Southern Hemisphere, causing the redistribution of heat from the Circumpolar Ocean to low latitude oceans. This reduction is indicated in Fig. 22, which illustrates the latitudinal profiles of the northward oceanic heat transport from the S, G, and D integrations. The poleward oceanic heat transport is reduced from the S to G integration in the Southern Hemisphere partly because of the intensification of the equatorward Ekman drift currents in middle latitudes, which results from the increase in surface westerlies explained in section 9a. This helps reduce the CO_2-induced heating of the vertical water column around 60°S latitude in the Circumpolar Ocean of the Southern Hemisphere, which is indicated in Fig. 21a.

In the Northern Hemisphere, the change in net surface heat flux is at a maximum at about 55°N latitude, dominated by the contribution from the northern North Atlantic. Again, the change in the surface heat flux is much larger than the change in the rate of oceanic heat storage, indicating the net removal of heat from this latitude by ocean currents. This is accomplished by the reduction of northward heat transport in the Atlantic where the thermohaline circulation is weakened, as discussed in section 9b. The reduction accounts for the decrease of the northward oceanic heat transport from the S to G integrations in the Northern Hemisphere as indicated in Fig. 22.

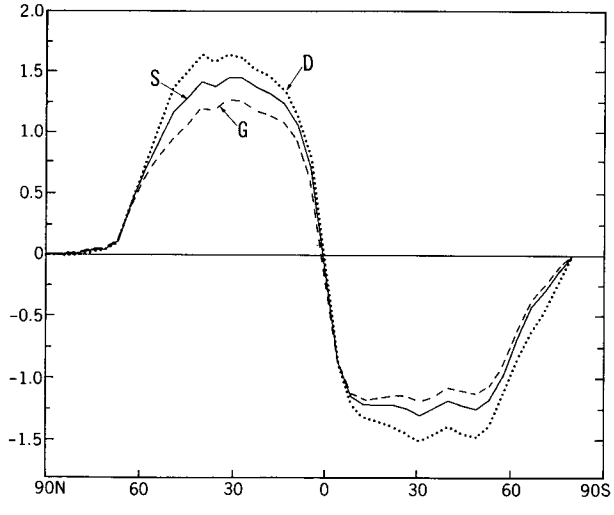

FIG. 22. The latitudinal profiles of the northward oceanic heat transport (10^{15} W) from the G, S, and D integrations. Here, the transport is computed indirectly from the heat budget of the model oceans.

Qualitatively similar features are evident in the oceanic heat budget from the CO_2 reduction experiment, although the CO_2-induced changes of both net surface heating and the rate of oceanic heat storage have opposite sign and tend to be somewhat larger than the changes obtained from the CO_2 growth experiment discussed above.

8. Hydrologic cycle and salinity change

Figure 23 illustrates the latitudinal profiles of zonal-mean rates of both precipitation and evaporation from the G, D, and S integrations. The rates represent the average over the 60th to 80th year of an experiment when the concentration of atmospheric carbon dioxide is doubled or halved in the G and D integration, respectively. By subtracting the results of the S from the G integration (or those of the S from the D integration), one can get the CO_2-induced change in the rates of precipitation and evaporation in response to the increase (or decrease) of atmospheric carbon dioxide. For reference, the zonal-mean rates of actual precipitation as estimated by Budyko (1963) are also plotted in the same figure.

This figure indicates that, as noted in many previous studies (e.g., Manabe and Wetherald 1975), the rates of both precipitation and evaporation increase, resulting from an increase of atmospheric carbon dioxide. However, the latitudinal profile of the CO_2-induced increase in precipitation rate is quite different from the corresponding profile of evaporation. Specifically, the change in evaporation rate decreases with increasing latitudes and is very small in high latitudes. On the other hand, the enrichment of the water vapor content of air accompanying the atmospheric warming enhances the poleward moisture transport, thereby causing a marked increase in precipitation rate in high latitudes. Accordingly, the excess of precipitation over evaporation also increases substantially in these latitudes and contributes to the reduction of salinity in the upper layer of model oceans, as described below. However, it is likely that the model overestimates these changes in view of its bias toward overestimating the precipitation in high latitudes. In the experiment in which atmospheric carbon dioxide is reduced gradually, poleward transport of moisture decreases, reducing the excess of precipitation over evaporation in high latitudes.

In Fig. 24, the latitudinal profiles of the changes in the rates of both precipitation and evaporation dis-

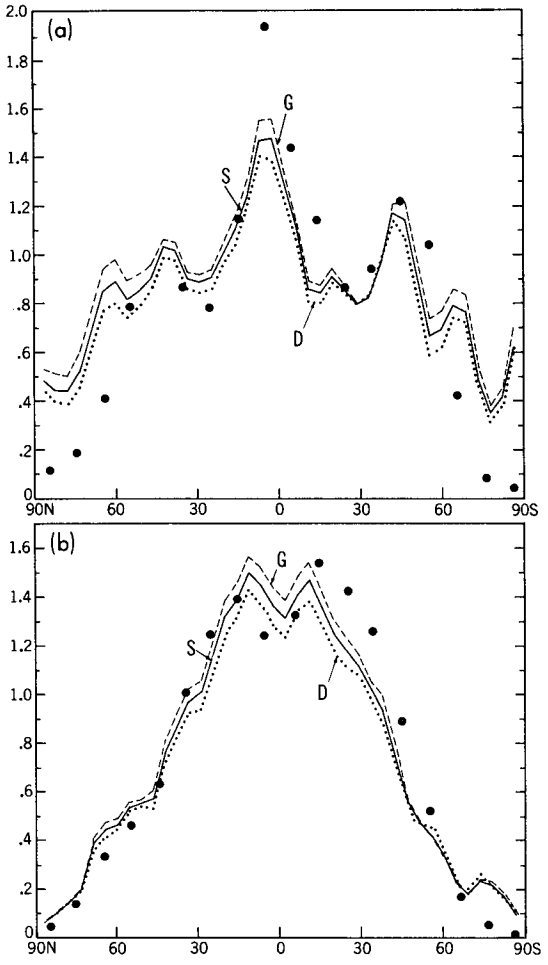

FIG. 23. The latitudinal profiles of zonal-mean rates (m yr^{-1}) of (a) precipitation and (b) evaporation averaged over the 60th to 80th year period of the G, S, and D integrations. The large dots indicate actual rates estimated by Budyko (1963).

cussed above are compared with the equilibrium response of these quantities to the doubling of atmospheric carbon dioxide. Here, only the results from the CO_2 growth experiment are compared for brevity of the discussion. In general, the increases of both precipitation and evaporation at the time of the CO_2 doubling in the transient response experiment are smaller than the corresponding increases in the equilibrium response experiment to the doubling. This is consistent with the difference in the CO_2-induced increase of surface temperature between the two experiments. It is of interest that, in the equilibrium response experiment, the CO_2-induced change in the rate of evaporation does not vary significantly between the low and middle latitudes, although it becomes very small in the polar regions. On the other hand, the rate decreases with increasing latitudes in the transient response experiment. In particular, it is very small in the Circumpolar Ocean of the Southern Hemisphere where the warming of the sea surface is very small.

The latitudinal profiles of the changes in precipitation rate shown in Fig. 24a are quite different from the corresponding profiles for evaporation rate discussed above. In both equilibrium and transient response experiments, the CO_2-induced changes of precipitation rate in high latitudes are generally larger than those in low latitudes. As explained already, the increase in the poleward transport of water vapor in the model atmosphere is responsible for this latitudinal contrast.

It is notable that, in the CO_2 growth experiment, the precipitation rate increases substantially in high latitudes of the Southern Hemisphere where the CO_2-induced surface warming is small. As indicated in Fig. 16a, significant midtropospheric warming occurs in high latitudes of the Southern Hemisphere, enhancing the penetration of warm, moisture-rich air toward the Antarctic Continent. Thus, the large excess of precipitation over evaporation should contribute to the accretion of the ice sheet over the continent.

The latitudinal profiles of zonally averaged, annual mean rates of runoff from the G, S, and D integrations are shown in Fig. 25. Again, the rates represent the averages over the 60th to 80th year period. To illustrate clearly the CO_2-induced changes, the difference between the G and S and the D and S integrations are shown in a magnified scale in the bottom half of the

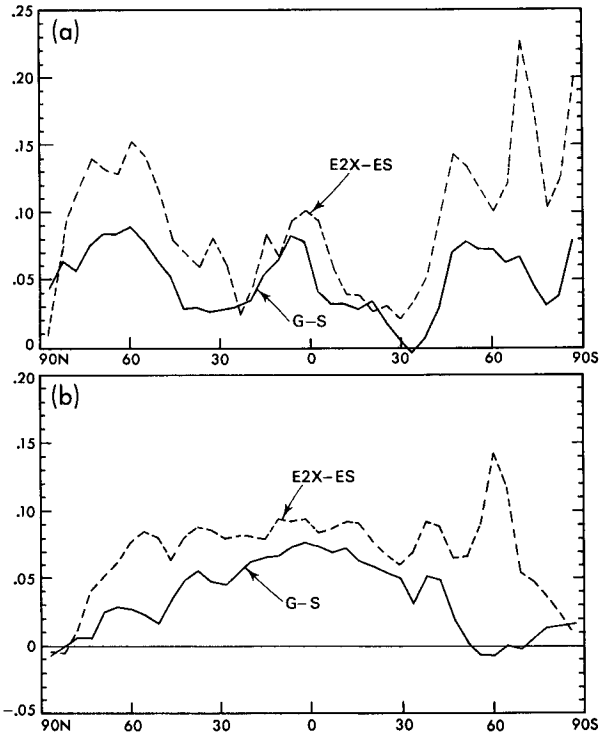

FIG. 24. (a) The latitudinal profiles of the difference in zonal-mean rate (m yr^{-1}) of precipitation between the G and S integration (solid line) and E2X and ES integration (dashed line). The rates from the G and S integrations represent an average over the 60th to 80th year period. (b) Same as above except that it indicates the difference in evaporation.

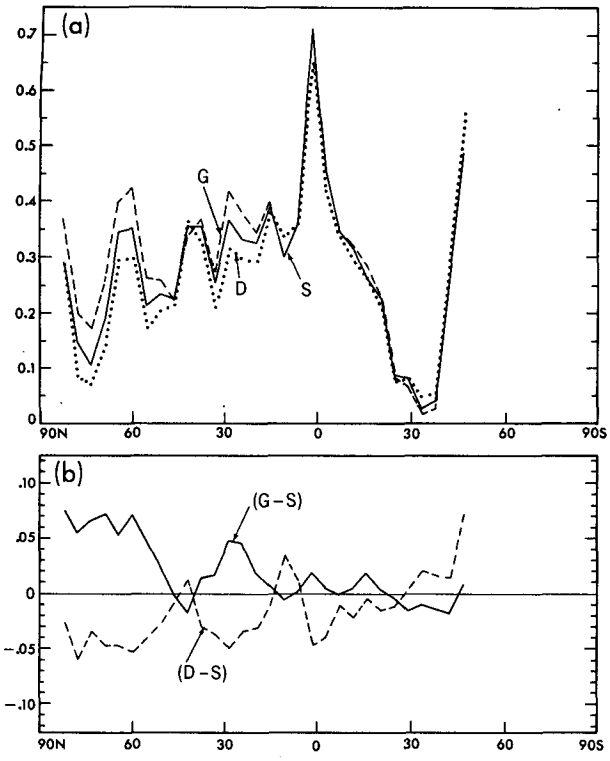

FIG. 25. (a) The latitudinal profiles of annually averaged zonal-mean rates (m yr^{-1}) of runoff from the G, S, and D integrations. (b) The latitudinal profiles of the difference in zonal-mean rates (m yr^{-1}) of runoff between G and S integrations (solid line) and D and S integrations (dashed line).

figure. A marked increase (reduction) of the runoff rate occurs in high latitudes of the Northern Hemisphere in response to the increase (reduction) of atmospheric carbon dioxide, contributing to the change in salinity in the upper layer of the Arctic Ocean as discussed below. Although it is not included as a part of runoff shown in Fig. 25, the runoff of ice from the Antarctic Continent to the surrounding oceans increases substantially in response to the increase of atmospheric carbon dioxide. This increase in ice runoff results from the assumption of the model that the net accretion of the ice sheet should not exceed 20 cm. Without this assumption, it would have contributed to the accumulation of ice over the Antarctic ice sheet.

As expected, the CO_2-induced change in the surface water flux affects the distribution of salinity in the upper layer of the ocean. The temporal variations of zonal-mean surface salinity, in response to the gradual increase and reduction of atmospheric carbon dioxide, are illustrated in the upper and lower half of Fig. 26, respectively. This figure indicates that, in the CO_2 growth experiment, zonal-mean salinity is reduced with time poleward of 45° latitude and increases very slightly equatorwards of this latitude. As noted earlier, the water flux at the oceanic surface (i.e., the excess of precipitation over evaporation) increases substantially in response to the increase of atmospheric carbon dioxide, thereby contributing to the reduction of surface salinity in high latitudes mentioned above. On the other hand, the water flux is reduced slightly in most of the low latitudes, causing the slight increase of surface salinity.

In the CO_2 reduction experiment, surface salinity changes are opposite to those in the CO_2 growth experiment. As discussed already, the surface water flux also changes in the opposite direction accounting for the latitudinal profile of change in surface salinity.

To examine the vertical structure of the salinity anomaly described above, the latitude–depth distributions of the CO_2-induced changes of zonal-mean surface salinity are illustrated in Fig. 27 for the cases of both increasing and decreasing concentration of atmospheric carbon dioxide. Each distribution represents the averages over the 60th to 80th years of an experiment. Examining the results from the CO_2 growth experiment, one notes that zonal-mean surface salinity is reduced substantially in the upper few hundred meters in high latitudes of the Northern Hemisphere. An inspection of the geographical distribution of the CO_2-induced surface salinity change indicates that the re-

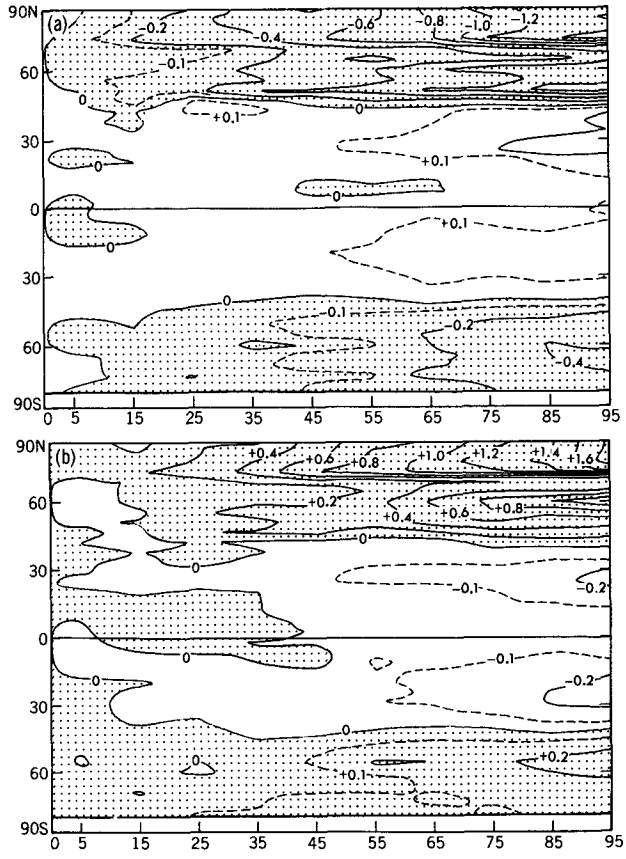

FIG. 26. The temporal variation of the difference in zonally averaged, decadal-mean surface salinity (psu) between (a) the G and S, and (b) D and S integrations.

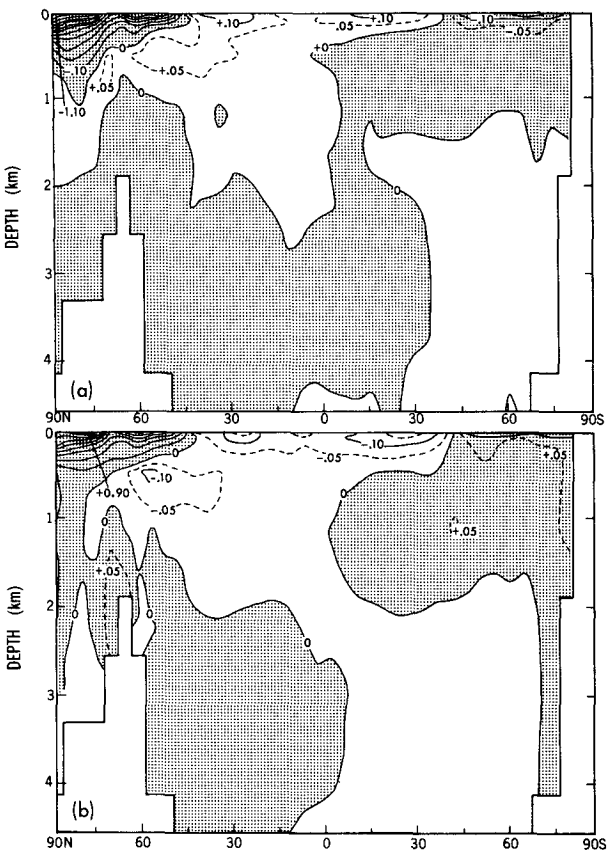

FIG. 27. The latitude–depth distribution of the difference in zonal-mean salinity (psu) between (a) G and S, and (b) D and S integrations.

duction is relatively large over the Arctic and the northern North Atlantic oceans. Over the Circumpolar Ocean, the reduction of zonal-mean salinity is essentially confined to the mixed layer and is smaller than the reduction in the Arctic Ocean. In the experiment in which atmospheric carbon dioxide is reduced with time, the change in zonal-mean salinity has a similar distribution but is opposite in sign. The similarity in distribution underscores the fact that the changes in salinity described here are CO_2-induced and are controlled by similar mechanisms.

As discussed in the following section, the CO_2-induced change in salinity described above alters the static stability and exerts a significant influence upon the intensities of the thermohaline circulation and vertical mixing in high latitudes. For example, in the CO_2 increase experiment, surface salinity decreases in high latitudes, thereby increasing the static stability and reducing the penetration depth of positive temperature anomalies. On the other hand, the reverse is the case in the CO_2 reduction experiment, enhancing the downward penetration of the negative anomaly in high latitudes. Thus, the effective thermal inertia of the model oceans in the former is substantially smaller than the latter, as noted in section 6. The CO_2-induced change of oceanic temperature also reduces the static stability of the upper ocean layer in low and middle latitudes, thereby exerting a similar influence upon the penetration depth and, accordingly, the thermal inertia of the model ocean.

9. Deep circulation and vertical mixing in the ocean

It was shown in section 6 that the changes of surface air temperature in response to a gradual increase (or reduction) of atmospheric carbon dioxide are particularly slow over the Circumpolar Ocean of the Southern Hemisphere and the northern North Atlantic where the vertical mixing of water penetrates very deeply. This section explores how the deep oceanic cells of meridional circulation and their changes control the vertical mixing of water and heat in these oceans, thereby affecting the CO_2-induced change of climate.

a. Circumpolar Ocean

Figure 28 illustrates the streamfunctions of zonal-mean meridional circulation from the G, S, and D integrations. They represent the time averages over the 60th to 80th year period of these integrations. All streamfunctions indicate a deep, wind-driven indirect cell in the 40° ~ 60°S latitudes where westerlies prevail not only in the upper troposphere, but also near the oceanic surface. The presence of deep water upwelling south of the Circumpolar current has been suggested based upon the analysis of water mass structure (Deacon 1937; Sverdrup et al. 1942). In addition to the indirect cell, each streamfunction contains a deep, direct cell in the coastal latitudes of the Antarctic Continent.

The deep intrusion of the indirect cell mentioned above results from the absence of a meridional barrier in the Southern Hemisphere at the latitudes of the Drake Passage. Bryan et al. (1988) investigated this issue by use of a coupled ocean–atmosphere model with a sector computational domain bounded by two meridians 120 degrees apart and an idealized sector geography. They compared the results from two versions of the model in which the Drake Passage is either closed or opened. In the version with the closed Drake Passage a zonal pressure gradient develops, maintaining the southward geostrophic flow beneath the northward Ekman drift currents, induced by the intense surface westerlies. On the other hand, the zonal pressure gradient is small in the version without the meridional barrier. Thus, the westerly-induced, equatorward Ekman drift can only be compensated by a deep downwelling north of the Drake Passage, southward geostrophic flow below the depth of the sill where a zonal pressure gradient can develop, and deep upwelling south of the Circumpolar Current. [Refer to the smoothed bottom topography in Fig. 2 of Manabe and Stouffer (1988) for the identification of a sill near the

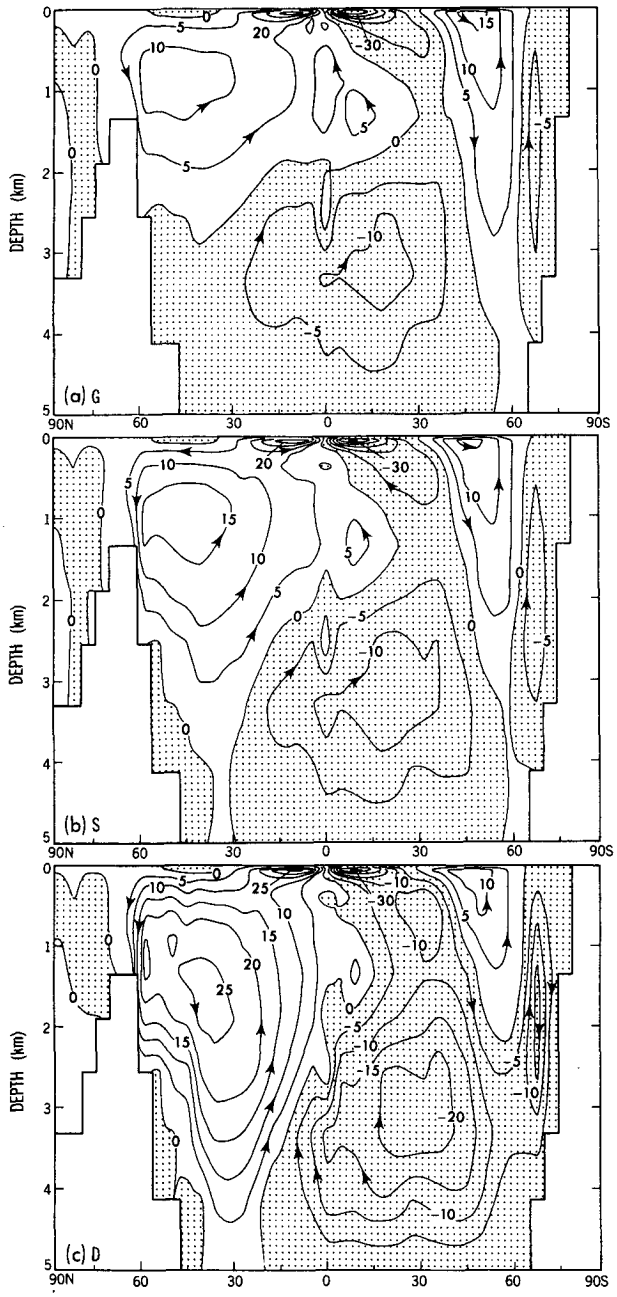

FIG. 28. The latitude–depth distribution of the streamfunction of meridional circulation over all oceans of the model. They represent the 20-year mean circulation averaged over the 60th to 80th year of (a) the G, (b) the S, and (c) the D integrations. Units are Sv $\equiv 10^6$ m^3 s^{-1}.

Drake Passage of the model.] As indicated in Fig. 16, a deep penetration of temperature anomaly is indicated poleward of 50°S in the upwelling branch of the wind-driven cell in both G and D integrations. Both thermal advection by the cell and induced convective overturning make the vertical mixing very effective in the upwelling region.

As noted earlier, another deep cell exists in the immediate vicinity of the Antarctic Continent. The large fluctuation of surface salinity, which mainly results from the temporal variation (including winter growth) of sea ice volume, induces the deep convection and associated thermohaline cell, thereby causing very effective vertical mixing in this region.

As noted by Manabe et al. (1990), the heat balance of the Circumpolar Ocean polewards of 55° in the present CO_2 growth experiment is also maintained as a balance between the heating due to the thermal advection by the deep cells and the cooling due to the deep convection and subgrid-scale mixing. Thus, heat is mixed very effectively to great depth, markedly reducing the warming in the near-surface layer of the model ocean and the overlying atmosphere.

Figure 28 indicates that the pattern of the meridional circulation in the model oceans is qualitatively similar among the S, G, and D integrations. However, the intensities of meridional circulation cells differ from one integration to another. For example, in response to the increase of atmospheric carbon dioxide, the meridional temperature gradient increases in the model troposphere of the Southern Hemisphere from the S to G integrations, intensifying the surface westerlies which, in turn, intensifies slightly the equatorial Ekman drift currents as a part of the indirect cell in middle latitudes. On the other hand, this cell weakens from the S to D integration in response to the reduction of atmospheric carbon dioxide because of the weakening of surface westerlies. The changes in the surface wind stress implied in the CO_2-induced changes of surface westerlies mentioned above are indicated around 50°S in Fig. 29.

Figure 28a also indicates that, in the immediate vicinity of the Antarctic Continent, the direct cell of meridional circulation weakens slightly from the S to the G integrations, whereas it intensifies from the S to D integrations. The latter change resulting from the reduction of atmospheric carbon dioxide is much larger than the former change caused by the CO_2 increase. The marked intensification of the cell from the S to D integrations appears to be attributable to the sinking of cold, relatively saline water, which results from the fluctuation of surface salinity due to the seasonal variation of sea ice. The intensification of the thermohaline circulation together with the increase in convective activity discussed below accounts for the deep penetration of the negative anomaly near the coast of the Antarctic Continent. The northward spreading of the bottom water thus produced is enhanced due to advection by the direct cell in the deep oceans of the Southern Hemisphere (see the cell centered around 30°S and at the depth of about 3 km in Fig. 28).

Although the efficient vertical mixing may be the most important factor responsible for the smallness of sea surface temperature change in the Circumpolar Ocean of the Southern Hemisphere, it does not explain

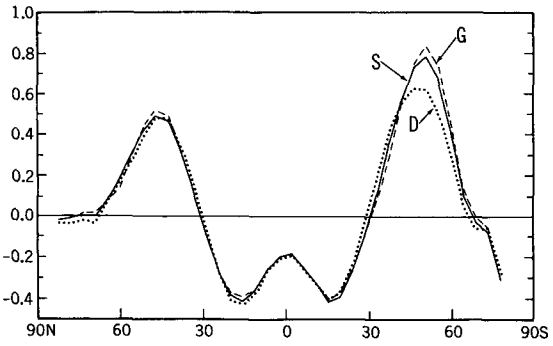

FIG. 29. The latitudinal profiles of zonal-mean wind stress (0.1 N m^{-2}) from the S, G and D integrations are indicated by solid, dashed, and dotted lines, respectively. The values are averaged over the 60th to 80th years of the integrations.

why the change is practically zero or sometimes reversed in sign. As noted by Manabe et al. (1990) based upon the detailed analysis of the heat budget of the Circumpolar Ocean of their model, the reduction of convective activity in the surface layer is responsible for this interesting phenomenon. For example, in response to the increase of atmospheric carbon dioxide, the excess of precipitation over evaporation increases, and surface salinity is reduced in high latitudes as noted in section 8. Thus, the static stability of the near-surface water increases and the convective mixing of cold surface water with the relatively warm subsurface water is reduced, thereby contributing to the reduction of sea surface temperature in the Circumpolar Ocean. This is why sea surface temperature hardly changes and sea ice slightly increases near the Antarctic Continent in response to the increase of atmospheric carbon dioxide. In the CO_2 reduction experiment, the opposite processes involving the increase in surface salinity and enhanced convective overturning of surface water prevents the cooling of sea surface temperature.

b. Atlantic Ocean

In section 6, it is noted that the change in sea surface temperature in response to the increase (or reduction) of atmospheric carbon dioxide is particularly small over an extensive region of the northern North Atlantic. To examine the vertical structure of the CO_2-induced thermal anomalies, the zonal-mean temperature difference of the Atlantic Ocean between the G and S (or D and S) integrations is time-averaged over the 60th to 80th year period and is illustrated in Fig. 30. For comparison, similar pictures are constructed for the Pacific Ocean, as is shown in Fig. 31.

According to Fig. 30, the downward penetration of the thermal anomalies in the Atlantic Ocean is particularly deep in the latitude belt between 60° and 75°N. The penetration is particularly deep in the case of decreasing atmospheric carbon dioxide. A similar tongue of deep penetration is not evident for the Pacific anomalies shown in Fig. 31. As discussed below, this difference in the penetration of thermal anomalies between the Atlantic and Pacific oceans is attributable to the existence of thermohaline circulation in the Atlantic Ocean and the absence of such circulation in the Pacific Ocean.

The streamfunctions of zonal-mean meridional circulation in the North Atlantic Ocean are averaged over the 60th–80th year period of the G, S, and D integrations and are shown in the upper, middle, and lower parts of Fig. 32. A comparison between this figure and Fig. 28 reveals that the meridional overturning in the Northern Hemisphere is essentially achieved in the Atlantic Ocean. It also indicates that the thermohaline circulation in the Atlantic Ocean becomes weaker and shallower from the S to the G integrations in response to the increase of atmospheric carbon dioxide, whereas it intensifies and deepens from the D and G integrations responding to the CO_2 reduction.

The CO_2-induced changes in thermohaline circulation of the Atlantic Ocean mentioned above result from the salinity change in the surface layer discussed in section 8. For example, as the atmospheric carbon dioxide increases, surface salinity is reduced in high

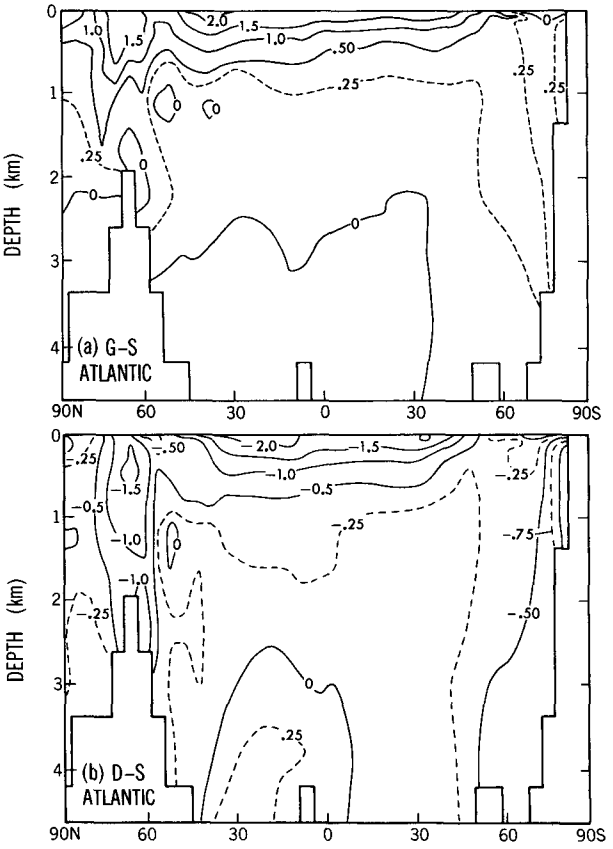

FIG. 30. The latitude–depth distribution of the zonal-mean difference of temperature (°C) in the Atlantic Ocean of the model between (a) the G and S integrations and (b) the D and S integrations.

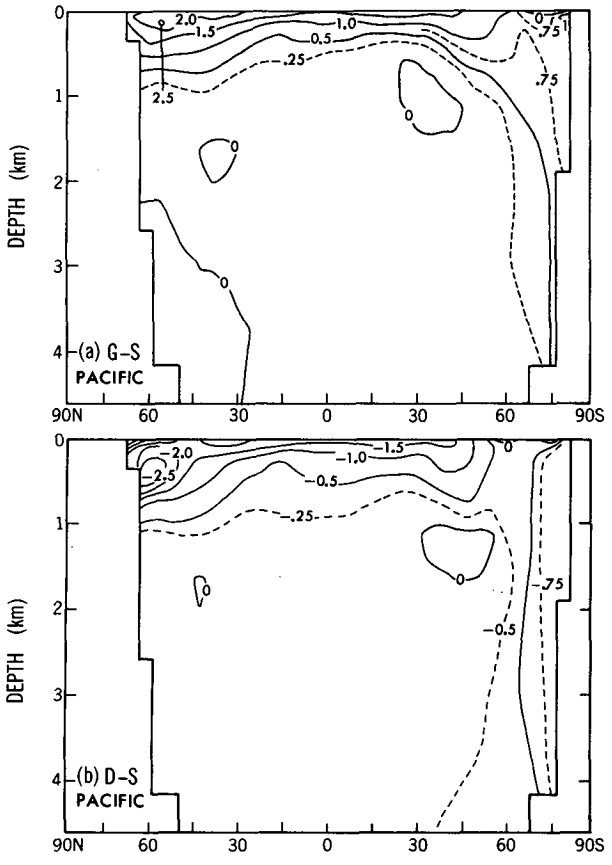

FIG. 31. Same as Fig. 30, but for the Pacific Ocean of the model.

latitudes due to the increase in excess precipitation over evaporation. The capping of the northern North Atlantic with relatively fresh near-surface water makes the thermohaline circulation weaker and shallower in the Atlantic Ocean. The reduction in the rate of deep-water formation resulting from the freshwater capping in the North Atlantic has been suggested, for example, by Broecker et al. (1985). The reverse situation is realized in the case of CO_2 reduction, causing the intensification and deepening of the thermohaline circulation.

Figure 32 indicates that the sinking branch of the thermohaline circulation described above is located in the northern North Atlantic where the downward penetration of a thermal anomaly is particularly pronounced (Fig. 17). In this sinking branch and its neighborhood, the heating due to the downward advection of relatively warm water is counterbalanced by the cooling due to convective overtuning, resulting in the effective vertical mixing of heat and the deep penetration of thermal anomalies described above. Thus, the heat trapped by the increasing atmospheric carbon dioxide, for example, is spread over a very deep water column, thereby markedly reducing the increase of sea surface temperature in the northern North Atlantic.

As Fig. 32 shows, the downward penetration of the thermohaline circulation in the northern North Atlantic is deeper in the D than the G integration. Accordingly, the vertical mixing of heat also penetrates deeper in the former than the latter. This is consistent with the fact that, in the northern North Atlantic, the penetration depth of the negative temperature anomaly in the CO_2 reduction experiment is larger than that of the positive anomaly in the CO_2 growth experiment as illustrated in Fig. 17.

In addition to the effective vertical mixing, there is another important factor that is responsible for making the surface warming small in the northern North Atlantic. In the case of increasing atmospheric carbon dioxide, for example, the weakening of the thermohaline circulation in the Atlantic reduces the northward advection of warm, saline surface water, causing a reduction of surface temperature immediately to the south of the region of sinking. The reduction of warm advection of surface water together with the intense vertical mixing are responsible for the extensive regions of relatively small warming located to the south of Greenland.

In the experiment with decreasing atmospheric carbon dioxide, the thermohaline circulation in the Atlantic Ocean intensifies as noted already, enhancing the northward advection of relatively warm surface water and counterbalancing the direct CO_2-induced cooling of surface water. This increase of warm advection together with the more efficient and deeper vertical mixing of water in the sinking branch of the thermohaline circulation again accounts for the extensive region of relatively small cooling in the northern North Atlantic as indicated in Fig. 14.

Over the North Pacific where the thermohaline circulation is very weak (or nonexistent), the vertical mixing of water is extremely slow and the downward penetration of the thermal anomaly is not pronounced in high latitudes. Thus, the sea surface warming in response to the increasing atmospheric carbon dioxide is widespread in the northern North Pacific. In the case of decreasing atmospheric carbon dioxide one notes, however, the region of relatively small surface cooling that appears in the Okhotsk Sea (see Fig. 15). This is due to the penetration of the negative thermal anomaly to intermediate depths in this region. As discussed in section 8, surface salinity increases in high latitudes where surface water flux decreases in the CO_2 reduction experiment. The increase of surface salinity together with the winter growth of sea ice, which causes brine formation and the sinking of water, are responsible for the efficient mixing in this region.

10. Summary and concluding remarks

It has been shown that, responding to a gradual increase of atmospheric carbon dioxide, the surface temperature of the coupled model increases very slowly in

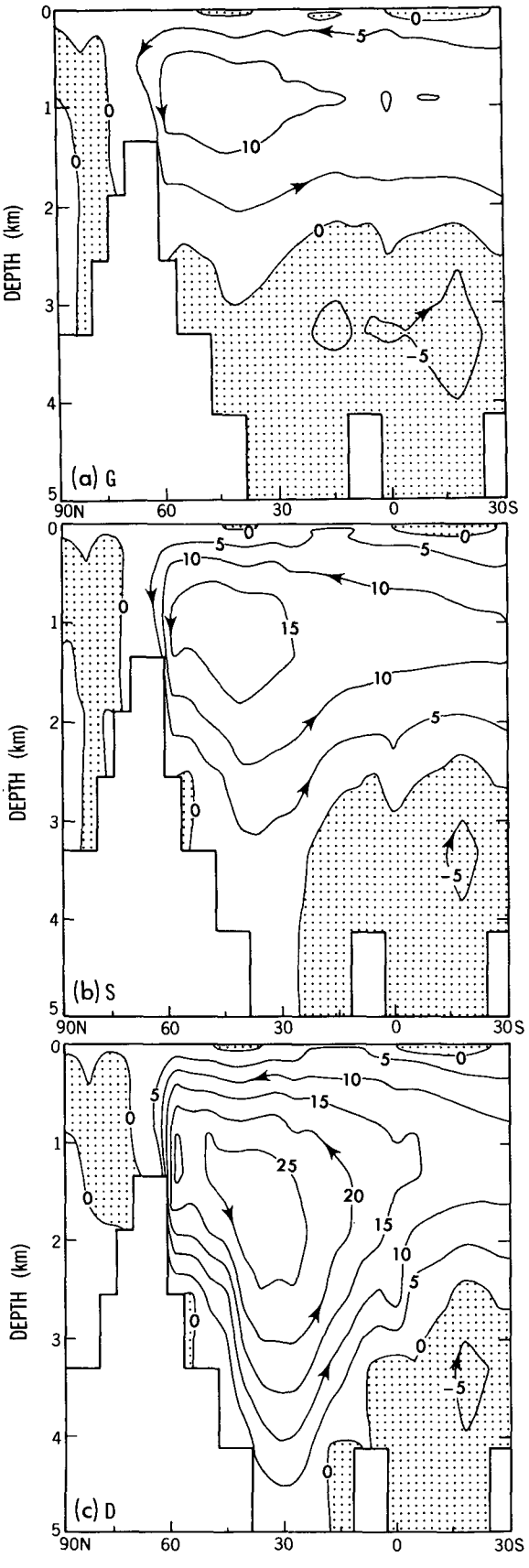

the Circumpolar Ocean of the Southern Hemisphere and the northern North Atlantic where sinking branches of the thermohaline circulation are located. As explained in this and earlier studies, the vertical mixing of water extends very deeply in these regions through the combined effect of thermal advection by ocean currents and vertical subgrid-scale mixing, including convection. Because of this deep vertical mixing, heat trapped by the increasing atmospheric carbon dioxide spreads deeply over a thick layer of water with large heat capacity, thereby making the warming of surface temperature very small in these oceanic regions.

In the northern North Atlantic, another process contributes to the reduction of CO_2-induced warming of the sea surface. Because of the increase in the moisture content of air that accompanies the warming of the troposphere, the poleward transport of water vapor increases, thereby increasing the positive surface water flux, i.e., the excess of precipitation over evaporation, in high latitudes. The increase of surface water flux, in turn, lowers salinity in the near-surface layer of the Arctic and surrounding oceans. This capping of the ocean by water with relatively low salinity and density results in weakening of the thermohaline circulation and the reduction of the northward advection of warm, saline surface water, thereby lowering the sea surface temperature. This reduction in the near-surface advection of warm water, together with the deep vertical mixing of heat mentioned earlier, produces a region of relatively small surface warming in the northern North Atlantic Ocean.

In the Circumpolar Ocean of the Southern Hemisphere, surface salinity is also reduced due to the increase of freshwater flux from the atmosphere. The reduction of salinity and density in the near-surface layer, in turn, weakens the convective mixing of cold surface water with the underlying warmer water, thereby lowering sea surface temperature. This near-surface process together with the deep vertical mixing of heat trapped by increasing greenhouse gas make the warming of the sea surface very small, sustaining the regions of no warming in the immediate vicinity of the Antarctic Continent.

There are other processes that contribute to the reduction of CO_2-induced warming in the Circumpolar Ocean. For example, the large areal coverage by oceans tends to reduce the heat storage per unit area. Another factor involves the meridional heat transport by ocean currents. Because of the CO_2-induced increase of the meridional temperature gradient in the model troposphere, the westerlies intensify, thereby increasing the equatorward Ekman drift of surface water and reducing

FIG. 32. The latitude–depth distribution of the streamfunctions of meridional circulation in the Atlantic Ocean of the model. They represent the 20-year mean circulations averaged over the 60th to 80th year of (a) the G, (b) the S, and (c) the D integrations. Units are Sv.

the poleward heat transport in middle latitudes. The net consequence is the removal of heat from the Circumpolar Ocean and the lowering of sea surface temperature.

The transient response of surface air temperature of the coupled ocean–atmosphere model at the time of CO_2 doubling is compared with the equilibrium response of an atmosphere–mixed-layer ocean model to the doubling. When computing the ratio of the former to the latter, one notes that the ratio is particularly small over the Circumpolar Ocean of the Southern Hemisphere and the northern North Atlantic as influenced by the processes identified above. However, with the exception of these two regions, the ratio ranges between 0.6 and 0.8 and does not vary much. This indicates that the geographical distribution of the equilibrium response of surface air temperature of an atmosphere–mixed-layer ocean model, which has been the subject of many previous studies, may be approximately similar to the distribution of the transient response of a coupled model over most of the Northern Hemisphere and the low latitudes of the Southern Hemisphere. For example, the large increase of surface air temperature over the Arctic and its surrounding areas is a common feature of both transient and equilibrium responses. As discussed in many previous studies, this polar amplification of the CO_2-induced warming in the Northern Hemisphere is attributable to the positive albedo feedback effects of snow and sea ice operating in the stable, near-surface layer of the atmosphere. One also notes that, in both transient and equilibrium responses, the increase of surface air temperature is significantly larger over the North American and Eurasian continents than over the Pacific and Atlantic oceans in middle latitudes. Although the very small warming over the northern North Atlantic in the transient response experiments is mainly attributable to the processes discussed earlier, the land–sea difference in warming is partly because the increase in evaporative ventilation from a warmer surface with higher saturation vapor pressure is larger over wet oceans than partially wet continents.

The change in the North Atlantic in response to an increase in atmospheric carbon dioxide has been the subject of increasing interest among climate modelers. For example, Washington and Meehl (1989) noted the weakening of the thermohaline cell in the Atlantic Ocean of their model. However, the sinking leg of the cell in their model is located in middle rather than high latitudes, making it difficult to evaluate the implication of this result in the CO_2-induced temperature change in the northern North Atlantic. Although Manabe et al. (1990) recently noted a slight weakening of the unrealistically weak thermohaline circulation in the Atlantic Ocean of their model, the change in its intensity is too small to have a major effect upon the CO_2-induced change in sea surface temperature of the Atlantic. Fortunately, the thermohaline circulation in the Atlantic Ocean of the present model has realistic intensity, encouraging us to evaluate the possible effect of the circulation and its change upon the CO_2-induced sea surface temperature change of the northern North Atlantic.

The small CO_2-induced surface warming in the Circumpolar Ocean of the Southern Hemisphere was first simulated by Bryan et al. (1988) by use of a coupled ocean–atmosphere model with a sector-shaped computational domain and idealized geography. Washington and Meehl (1989) found that the increase of surface air temperature in the Circumpolar Ocean of their global model is somewhat smaller than the warming at the corresponding latitudes in the Northern Hemisphere. However, the interhemispheric difference is much less evident in their experiment, probably because the surface westerlies, the wind-driven deep cell, and accordingly, the vertical mixing of water in the Circumpolar Ocean are underestimated in their simulation. The effect of an enhanced pycnocline upon the temperature change at the surface of the Circumpolar Ocean was first emphasized by Manabe et al. (1990) based upon the results from a global ocean–atmosphere model without the seasonal variation of insolation. The present study shows that qualitatively similar results are obtained by a seasonal model, despite the seasonal fluctuation in the near-surface condition of the Circumpolar Ocean.

In addition to the CO_2 growth experiment described above, we conducted another experiment in which the atmospheric carbon dioxide is reduced at an exactly identical rate. It was found that the geographical distribution of the surface air temperature reduction in this CO_2 reduction experiment is approximately similar to the distribution of the warming from the CO_2 growth experiment. However, the downward penetration of the cold anomaly in the former is generally deeper than that of the penetration of the warm anomaly in the other experiment. In the CO_2 reduction experiment, surface salinity increases and static stability is reduced in high latitudes. Accordingly, the downward penetration of the cold anomaly is enhanced, particularly over the northern North Atlantic and Circumpolar Ocean of the Southern Hemisphere where the deep-water formation predominates. Due to the reduction of near-surface temperature, the static stability of the upper ocean layers also decreases in middle and low latitudes, again enhancing the downward penetration of the cold anomaly. Thus, the effective thermal inertia of the ocean in the CO_2 reduction experiment is substantially larger than that in the CO_2 growth experiment at all latitudes.

It is notable, however, that the time-dependent response of the global-mean surface air temperature in the CO_2 reduction experiment is similar in magnitude to the corresponding response in the CO_2 growth experiment, despite the difference in the effective thermal inertia mentioned above. In the former experiment

with colder climate, snow and sea ice with high surface albedo cover a much larger area, thereby enhancing their positive feedback effect upon surface air temperature. On the other hand, surface cooling is reduced due to the larger effective thermal inertia of the oceans. Because of the compensation between these two factors, the magnitude of surface air temperature response turned out to be similar between the two experiments.

It is likely that the equilibrium response of the global-mean surface air temperature of the present coupled ocean–atmosphere model to the doubling of atmospheric carbon dioxide is not very different from that of the atmosphere–mixed-layer model, which is about 4°C. This value is significantly larger than 2.5°C, which was recently chosen as the most likely value by the Intergovernmental Panel on Climate Change (1990). The quantitative aspects of the results from the transient response experiment conducted here should be evaluated with this difference in mind.

It has been shown that, in response to the gradual reduction of atmospheric carbon dioxide, thermohaline circulation intensifies and the rate of deep-water formation increases in the North Atlantic Ocean, mainly due to the increased salinity in the near-surface layer of the ocean in high latitudes. This appears to be contradictory with faunal, isotopic, and chemical analysis of deep-sea cores, which indicate the weak or nonexistent deep-water formation in the last ice age (see, for example, Broecker et al. 1985). One should not, however, compare the transient response over ten decades to the ice age response, which occurred on a much longer time scale when the communication with marginal seas such as the Greenland, Iceland, Norwegian, and Mediterranean seas was quite different from today.

The recent study of the deep-water circulation during the Neogene by Blanc and Duplessy (1982) may be relevant to this issue. They noted that the present pattern of thermohaline circulation was initiated approximately 13.2 million years ago when the Scotland–Faeroe–Iceland–Greenland ridge sufficiently subsided to allow the southward flow of the Arctic bottom water, as well as the northward surface flow of relatively saline water. Although it is likely that the reduction of the positive water flux in high latitudes in this cold climate may contribute as discussed in the present study, the lowering of the ridge may be responsible for the intensification of the thermohaline circulation in the Atlantic during the late Tertiary. On the other hand, the reverse situation may have occurred during the last glacial period. Because of the reduction of sea level and the increase of large icebergs, the meridional exchange of water and heat over the ridge might be reduced markedly, forming an iceshelf extending over the Norwegian and Greenland seas (e.g., Denton and Hughes 1981). This ice blockage may have impeded the water flow over the ridge enough to make the thermohaline circulation in the North Atlantic weaker. Further analysis of paleoclimatic signatures and modeling studies of the dynamical effect of the ridge are needed to confirm or reject this speculation.

In conclusion, the results from the present study indicate that the oceans can exert a profound influence upon the distribution of the CO_2-induced change of surface air temperature, although many of the features of the equilibrium response obtained from the previous studies still remain valid in most of the Northern Hemisphere and lower latitudes of the Southern Hemisphere. As discussed above, the effective thermal inertia of the oceans as influenced by oceanic circulation is particularly large over the northern North Atlantic and its surroundings and over the Circumpolar Ocean of the Southern Hemisphere where the CO_2-induced temperature change is small.

Obviously the credibility of the present study depends critically upon the ability of the present model to mimic the behavior of the actual ocean–atmosphere–land surface system. In this connection, it is encouraging that Dixon et al. (personal communication) recently succeeded in reproducing the downward spreading of chlorofluorocarbons in the Circumpolar Ocean of the Southern Hemisphere by employing the coupled model used in the present study. However, the surface flux adjustments of heat and water, which are needed to simulate the condition of the oceanic surface, are as large as those fluxes themselves. For example, the model tends to overestimate the precipitation in high latitudes and is partly responsible for the relatively large water flux adjustment needed there. It is possible that such a model bias results in the overestimation of the CO_2-induced change of precipitation, and accordingly, the changes of near-surface salinity and thermohaline circulation. Further improvements of the oceanic as well as the atmospheric component of the coupled model are urgently needed. In particular, the computational resolution of the model used here is too coarse to resolve the bottom topography and ocean currents, which have a dominating influence upon the response of a model to external forcing.

Acknowledgments. K. Dixon made available the latest version of the oceanic model and helped incorporate it into the coupled model used in the present study. N.-C. Lau, R. Toggweiler, and W. R. Holland reviewed the manuscript and gave valuable comments. J. Risbey made a major effort in critically examining the entire paper in great detail, giving many constructive recommendations. J. Kennedy and P. Tunison helped in the preparation of the manuscript and figures. J. D. Mahlman, Director of the Geophysical Fluid Dynamics Laboratory of NOAA, gave wholehearted support throughout the course of this study.

APPENDIX A

Representation of Mixing in the Ocean Model

The ocean component of the climate model is similar to that of Bryan and Lewis (1979), but the details of

the mixing of heat, salinity, and momentum due to subgrid scale eddies are somewhat different. The coefficients for the horizontal mixing of momentum, A_{mh}, and the vertical mixing of momentum, A_{mv}, are constants independent of depth. Mixing of heat and salinity has been parameterized in a more complex way. Basically two types of diffusion have been employed. One is a background horizontal and vertical diffusion as in the Bryan and Lewis (1979) model. The other is an additional mixing of heat and salinity parallel to surfaces of constant density and is intended to simulate the effect of macroscale eddies (Bryan 1987). The vertical background diffusion A_{hv} has the following dependence on the vertical coordinate:

$$A_{hv} = A_0 + \left(\frac{C_r}{\pi}\right) \tan^{-1}[0.0045 \times (Z - 2500)], \quad \text{(A1)}$$

where Z is the depth in meters. The background horizontal diffusion, A_{hh}, is independent of depth. The coefficient of the isopycnal diffusion is at a maximum in the upper thermocline and decreases with depth. It is given by the following formula,

$$A_{hi} = A_b + (A_s - A_b) \exp(-Z/500). \quad \text{(A2)}$$

Details of the isopycnal mixing formulation are given in Redi (1982) and Cox (1987). In addition to this subgrid scale mixing, the convective adjustments of temperature and salinity are performed iteratively as specified by Cox (1984). See Table A1 for the values of the mixing coefficients and constants contained in Eqs. (A1) and (A2).

APPENDIX B

Flux Adjustment

As described in section 3b, the adjustments of surface fluxes of heat and water are determined from the atmospheric and oceanic legs of the preliminary integration. The adjustments, which vary seasonally and geographically, are performed at the oceanic surface throughout the integration of a coupled model. Figure A1a illustrates the latitudinal profiles of the net downward zonal-mean fluxes of heat before and after the adjustment as averaged over the 100 years of the standard (S) integration. The difference between the two fluxes in this figure indicates the adjustment performed. Averaged over the entire model oceans, the heat flux is negative before the adjustment. However, it becomes very close to zero after the adjustment. This implies that, without the adjustment, the climate of the model would have been too cold. This cold bias is attributable to the tendency of the cloud prediction scheme in the model toward overestimating low cloud and underestimating high cloud. The magnitude of the adjustment is particularly large in the subtropics where the total cloudiness is overestimated over the oceans and, accordingly, the surface absorption of solar radiation is underestimated by the model. The overestimation of subtropical cloudiness results from the bias of the present model toward underestimating the intensity of the Hadley cell.

The latitudinal profiles of net downward water flux, zonally averaged over the oceanic segment, are illustrated in Fig. A1b. Again, the fluxes before and after the adjustment are given, averaged over the 100 years of the S integration. Contrary to the situation of heat flux, the water flux averaged over the entire global

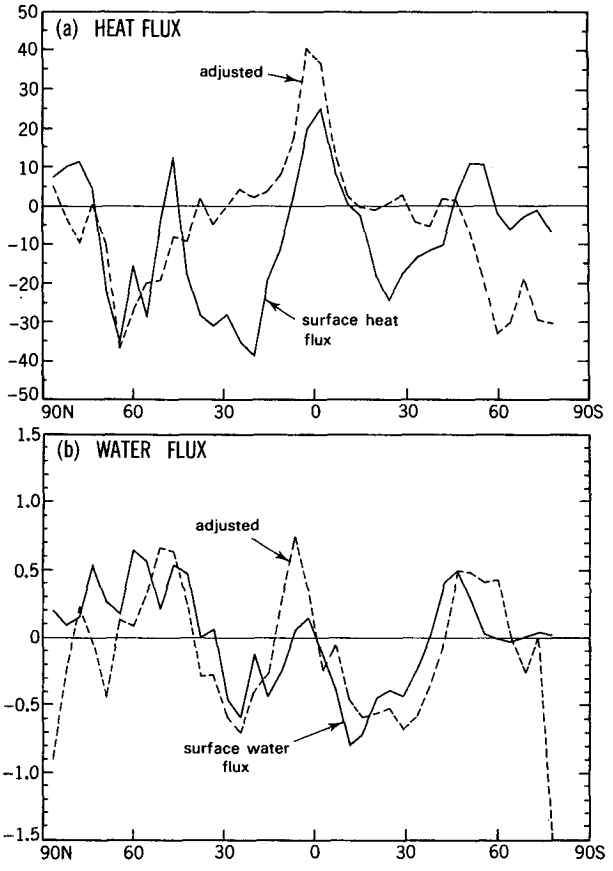

FIG. A1. The latitudinal profiles of net ocean-surface flux before and after the adjustment in the S integration of the coupled model. (a) Heat flux (W m^{-2}). (b) Water flux (m yr^{-1}). The fluxes are zonal means over the ocean, averaged over the 100-year period of the integration.

TABLE A1. Mixing parameters of the ocean model. Units: m^2 s^{-1}.

A_{mh}	horizontal viscosity	2.5×10^5
A_{mv}	vertical viscosity	5.0×10^{-3}
A_{hh}	horizontal diffusion	7.5×10^2
A_0	vertical diffusion coefficient	0.8×10^{-4}
C_r	vertical diffusion coefficient	1.05×10^4
A_b	isopycnal diffusion coefficient	5.0×10^3
A_s	isopycnal diffusion coefficient	4.0×10^3

oceans is close to zero before and after the adjustment. However, it is disturbing that a large negative adjustment of water flux is made in high latitudes of the Northern Hemisphere. Such a large adjustment is needed, partly because the present atmospheric model with relatively low computational resolution tends to overestimate the poleward atmospheric transport of moisture and, accordingly, the excess of precipitation over evaporation in high latitudes. It may be also attributable to the inability of a low-resolution ocean model with high subgrid-scale diffusion to bring sufficiently saline water to the northern North Atlantic where the sinking branch of the thermohaline circulation is located.

Figure A1b also indicates that the water flux adjustment is positive in the tropics, whereas it is negative in the subtropics. Again, the underestimation of the intensity of the Hadley cell mentioned earlier results in the underestimation of the precipitation rate in the tropics and the evaporation rate in the subtropics, making it necessary to adjust the water flux as described above.

It has been noted that, in an atmospheric component of the model with higher horizontal resolution, the convergence of moisture toward the polar region is smaller and the intensity of the Hadley cell is stronger. When the resolution of the oceanic component of the model is increased, the coefficient of subgrid-scale diffusion is smaller, possibly enhancing the advection of saline water toward the northern North Atlantic. Thus, it is expected that the adjustments of both heat and water fluxes would be smaller in a coupled model with higher resolution. The preparation of a numerical experiment with such a model is in progress.

REFERENCES

Blanc, P. L., and J. C. Duplessy, 1982: The deep-water circulation during the Neogene and the impact of the Messinian salinity crisis. *Deep-Sea Res.*, **29**, 1391–1414.

Broccoli, A. J., and S. Manabe, 1987: The influence of continental ice, atmospheric CO_2, and land albedo on the climate of the last glacial maximum. *Climate Dyn.*, **1**, 87–99.

Broecker, W., D. Peteet and D. Rind, 1985: Does the ocean–atmosphere system have more than one stable mode of operation? *Nature*, **315**, 21–26.

Bryan, K., 1969: Climate and the ocean circulation. III: The ocean model. *Mon. Wea. Rev.*, **97**, 806–827.

——, 1984: Accelerating the convergence to equilibrium of ocean-climate models. *J. Phys. Oceanogr.*, **14**, 666–673.

——, 1987: Potential vorticity in models of the ocean circulation. *Quart. J. Roy. Meteor. Soc.*, **113**, 713–734.

——, and L. J. Lewis, 1979: A water mass model of the world ocean. *J. Geophys. Res.*, **84** (C5), 2503–2517.

——, S. Manabe and R. C. Pacanowski, 1975: A global ocean–atmosphere climate model. II: The oceanic circulation. *J. Phys. Oceanogr.*, **5**, 30–46.

——, F. G. Komro, S. Manabe and M. J. Spelman, 1982: Transient climate response to increasing atmospheric carbon dioxide. *Science*, **215**, 56–58.

——, S. Manabe and M. J. Spelman, 1988: Interhemispheric asymmetry in the transient response of a coupled ocean–atmospheric model to a CO_2 forcing. *J. Phys. Oceanogr.*, **18**, 851–867.

Budyko, M. I., 1963: Atlas Teplovogo Balansa Zemnogo Shara (Atlas of the Heat Balance of the Earth). Glavnaia Geofys. Observ., Moscow, 69 pp.

Cox, M. D., 1984: A primitive equation, three-dimensional model of the ocean. GFDL Ocean Group Tech. Rep. No. 1, GFDL, Princeton University, Princeton, NJ.

——, 1987: Isopycnal diffusion in a *Z*-coordinate ocean model. *Ocean Modeling*, **74**, 1–5.

Crutcher, H. L., and J. M. Meserve, 1970: Selected level heights, temperatures, and dew points for the Northern Hemisphere. NAVAIR 50-1C-52, U.S. Naval Weather Service, Washington, D.C.

Deacon, G. E. R., 1937: Note on the dynamics of the southern Ocean. *Discovery Reports*, Cambridge University Press, 15, 125–152.

Denton, G. H., and T. J. Hughes, 1981: The Arctic ice sheet: An outrageous hypothesis. *The Last Great Ice Sheets*, G. H. Denton and T. J. Hughes, Eds., John Wiley, 440–467.

Dixon, K. W., J. L. Bullister, R. H. Gammon, R. J. Stouffer and G. P. J. Thiele, 1991: Climate model simulation studies using chlorofluoromethanes as transient oceanic traces. *Science*, submitted.

Gordon, C. T., and W. Stern, 1982: A description of the GFDL global spectral model. *Mon. Wea. Rev.*, **110**, 625–644.

Hansen, J., A. Lacis, D. Rind, G. Russell and P. Stone, 1984: Climate Sensitivity: Analysis of feedback mechanisms. *Climate Processes and Climate Sensitivity, Geophys. Monogr., No. 29*, Maurice Ewing, Vol. 5, J. E. Hansen and T. Takahashi, Eds. Amer. Geophys. Union, 130–163.

——, I. Fung, A. Lacis, D. Rind, S. Lebedeff, R. Ruedy, G. Russell and P. Stone, 1988: Global climate changes as forecast by the Goddard Institute for Space Studies three-dimensional model. *J. Geophys. Res.*, **93**, 9341–9364.

Harvey, L. D., and S. H. Schneider, 1985: Transient climate response to external forcing on 10^0–10^4 year time scales. Part I: Experiment with globally averaged, coupled atmosphere and ocean energy balance model. *J. Geophys. Res.*, **90**(D1), 2191–2205.

Hoffert, M. I., A. J. Callegari and C.-T. Hsieh, 1980: The role of deep sea storage in the secular response to climate forcing. *J. Geophys. Res.*, **85**, 6667–6679.

Intergovernmental Panel on Climate Change, 1990: Scientific assessment of climate change, 366 pp., WMO-UNEP.

Levitus, S., 1982: *Climatological Atlas of the World Ocean.* NOAA Prof. Paper No. 13, U.S. Dept. of Commerce, Washington, DC, 173 pp.

Manabe, S., 1969: Climate and the ocean circulation: I. The atmospheric circulation and the hydrology of the earth's surface. *Mon. Wea. Rev.*, **97**, 739–774.

——, and R. T. Wetherald, 1975: The effect of doubling CO_2 concentration on the climate of a general circulation model. *J. Atmos. Sci.*, **32**, 3–15.

——, and R. J. Stouffer, 1988: Two stable equilibria of a coupled ocean–atmosphere model. *J. Climate*, **1**, 841–866.

——, J. Smagorinsky and R. F. Strickler, 1965: Simulated climatology of a general circulation model with a hydrologic cycle. *Mon. Wea. Rev.*, **93**, 769–798.

——, K. Bryan and M. J. Spelman, 1990: Transient response of a global ocean–atmosphere model to a doubling of atmospheric carbon dioxide. *J. Phys. Oceanogr.*, **20**, 722–749.

Parkinson, C. L., J. C. Comiso, H. J. Zwally, D. J. Cavalieri, P. Gloersen and W. J. Campbell, 1987: Arctic Sea Ice, 1973–1976: Satellite passive-microwave observations. NASA SP-489, National Aeronautics and Space Administration, 296 pp.

Posey, J. W., and P. F. Clapp, 1964: Global distribution of normal surface albedo. *Geofis. Int.*, **4**, 33–48.

Redi, M. H., 1982: Oceanic isopycnal mixing by coordinate rotation. *J. Phys. Oceanogr.*, **12**, 1154–1158.

Roemmich, D., and C. Wunsch, 1984: Apparent changes in the climatic state of the deep North Atlantic. *Nature*, **307**, 447–450.

Schlesinger, M. E., W. L. Gates and Y. J. Han, 1985: The role of the ocean in CO_2-induced climatic warming: Preliminary results from the OSU coupled atmosphere–ocean GCM. *Coupled*

Ocean–Atmosphere Models, J. C. J. Nihoul, Ed., Elsevier, 447–478.

Smagorinsky, J., S. Manabe and R. F. Strickler, 1965: Simulated climatology of a general circulation model with a hydrologic cycle. *Mon. Wea. Rev.,* **93,** 769–798.

Spelman, M. J., and S. Manabe, 1984: Influence of oceanic heat transport upon the sensitivity of a model climate. *J. Geophys. Res.,* **89,** 571–586.

Street-Perrot, F., and R. Perrot, 1990: Abrupt climate fluctuations in the tropics: The influence of Atlantic Ocean circulation. *Nature,* **343,** 607–612.

Stouffer, R. J., S. Manabe and K. Bryan, 1989: Interhemispheric asymmetry in climate response to a gradual increase of atmospheric CO_2. *Nature,* **342,** 660–662.

Sverdrup, H. U., M. W. Johnson and R. H. Fleming, 1942: *The Oceans: Their Physics, Chemistry and General Biology.* Prentice Hall, 1087 pp.

Taljaard, J. J., H. van Loon, H. L. Crutcher and R. L. Jenne, 1969: Climate of the upper air, Part I. Southern Hemisphere, Vol. 1, Temperatures, dewpoints, and heights at selected pressure levels. NAVAIR 50-1C-55, U.S. Naval Weather Service, Washington, D.C.

Thompson, S. L., and S. H. Schneider, 1982: Carbon dioxide and climate: The importance of realistic geography in estimating the transient temperature response. *Science,* **217,** 1031–1033.

Washington, W. M., and G. A. Meehl, 1989: Climate sensitivity due to increased CO_2: Experiments with a coupled atmosphere and ocean general circulation model. *Climate Dyn.,* **4,** 1–38.

Zwally, H. J., C. Comiso, C. L. Parkinson, W. J. Campbell, F. D. Carsey and P. Gloersen, 1983: Antarctic Sea Ice, 1973–1976: Satellite passive-microwave observations. NASA SP-459, National Aeronautics and Space Administration, 206 pp.